JGR Solid Earth

RESEARCH ARTICLE
10.1029/2021JB022865

Strong Upper-Plate Heterogeneity at the Hikurangi Subduction Margin (North Island, New Zealand) Imaged by Adjoint Tomography

Bryant Chow[1,2,3], Yoshihiro Kaneko[4], Carl Tape[5], Ryan Modrak[6], Nick Mortimer[2], Stephen Bannister[2], and John Townend[1]

[1]School of Geography, Environment and Earth Sciences, Victoria University of Wellington, Wellington, New Zealand, [2]GNS Science, Lower Hutt, New Zealand, [3]Now at University of Alaska Fairbanks, Fairbanks, AK, USA, [4]Department of Geophysics, Kyoto University, Kyoto, Japan, [5]Geophysical Institute, University of Alaska Fairbanks, Fairbanks, AK, USA, [6]Los Alamos National Laboratory, Los Alamos, NM, USA

This article is a companion to Chow et al. (2022), https://doi.org/10.1029/2021JB022866.

Key Points:

- We develop a high-resolution (4–30 s) 3D velocity model of the North Island of New Zealand with 28 adjoint tomography iterations
- Distinct *P*- and *S*-wave velocity changes of up to ±30% are made to the existing model in the upper 30 km
- The tomographic results provide improved images of tectonic and magmatic structures throughout the Hikurangi subduction margin

Supporting Information:

Supporting Information may be found in the online version of this article.

Correspondence to:

B. Chow,
bhchow@alaska.edu

Citation:

Chow, B., Kaneko, Y., Tape, C., Modrak, R., Mortimer, N., Bannister, S., & Townend, J. (2022). Strong upper-plate heterogeneity at the Hikurangi subduction margin (North Island, New Zealand) imaged by adjoint tomography. *Journal of Geophysical Research: Solid Earth*, *127*, e2021JB022865. https://doi.org/10.1029/2021JB022865

Received 21 JUL 2021
Accepted 9 DEC 2021

Abstract We use earthquake-based adjoint tomography to invert for three-dimensional structure of the North Island, New Zealand, and the adjacent Hikurangi subduction zone. The study area, having a shallow depth to the plate interface below the North Island, offers a rare opportunity for imaging material properties at an active subduction zone using land-based measurements. Starting from an initial model derived using ray tomography, we perform iterative model updates using spectral element and adjoint simulations to fit waveforms with periods ranging from 4–30 s. We perform 28 model updates using an L-BFGS optimization algorithm, improving data fit and introducing *P*- and *S*-wave velocity changes of up to ±30%. Resolution analysis using point spread functions show that our measurements are most sensitive to heterogeneities in the upper 30 km. The most striking velocity changes coincide with areas related to the active Hikurangi subduction zone. Lateral velocity structures in the upper 5 km correlate well with New Zealand geology. The inversion reveals increased along-strike heterogeneity on the margin. In Cook Strait we observe a low-velocity zone interpreted as deep sedimentary basins. In the central North Island, low-velocity anomalies are linked to surface geology, and we relate velocity structures at depth to crustal magmatic activity below the Taupō Volcanic Zone. Our velocity model provides more accurate synthetic seismograms with respect to the initial model, better constrains small (<50 km), shallow (<15 km) and near-offshore velocity structures, and improves our understanding of volcanic and tectonic structures related to the active Hikurangi subduction zone.

Plain Language Summary We perform seismic imaging of the Earth's crust below the North Island of New Zealand, which sits above an active plate boundary known as the Hikurangi subduction zone. By comparing computer simulations of earthquake ground motion with recordings of ground motion, our imaging method iteratively improves models of Earth's subsurface structure. Our data set consists of earthquake waveforms from 1,800 unique source–receiver pairs. We incrementally update the seismic velocities of the initial model 28 times, resulting in velocity changes of up to ±30%. Variations in the subsurface structure are most strongly resolved in the upper 30 km. Seismic velocity structures in the upper 5 km correspond well with known surface geology. The strongest velocity changes correspond to regions related to the Hikurangi subduction zone, such as a deep sedimentary basin in Cook Strait, and anomalous velocity structures related to the Taupō Volcanic Zone. The newly derived velocity model improves predictions of earthquake ground motion and improves our understanding of volcanic and tectonic structures associated with the active Hikurangi subduction zone.

1. Introduction

In New Zealand, ray-based seismic tomography has produced detailed images of an active convergent plate boundary (Eberhart-Phillips & Bannister, 2015; Eberhart-Phillips, Bannister, Reyners, et al., 2020; Eberhart-Phillips et al., 2005; Eberhart-Phillips & Reyners, 2012). These tomographic images have been used for earthquake relocation studies (e.g., Bannister et al., 2011; Lanza et al., 2019; Reyners et al., 2011), ground motion simulations (e.g., Bradley et al., 2017; Chow et al., 2020; Kaneko et al., 2019), and characterization of structures, material properties, and slip behavior related to the Hikurangi subduction zone (e.g., Ellis et al., 2017; Henrys et al., 2020; Reyners et al., 2017; Williams et al., 2013; Williams & Wallace, 2018). These images have

also improved knowledge related to the potential for large, megathrust earthquakes that pose significant risk to New Zealand and the surrounding regions (e.g., D. Barker et al., 2009; Cochran et al., 2006; Eberhart-Phillips et al., 2005; Fagereng & Ellis, 2009; Henrys et al., 2006; Kaneko et al., 2018; Litchfield et al., 2007; Reyners et al., 2006; Wallace & Beavan, 2006; Wallace et al., 2009; Wallace et al., 2014). Despite their wide utility, these models are derived using ray theory, which has been shown to lead to ambiguous interpretations of tectonic features (Dahlen & Baig, 2002; Dahlen et al., 2000; Hung et al., 2001; Marquering et al., 1999; Zhao et al., 2000). Modern advances in computational power, and progress in the field of seismic tomography, have ushered in an era of imaging using full-waveform techniques. These techniques rely on seismic wavefield simulations, and they measure all or part of the time-dependent seismic waveform, rather than point measurements like traveltime differences. Taking advantage of full-waveform tomography, this study seeks to improve a ray-based velocity model of the North Island of New Zealand.

Adjoint tomography is a type of full-waveform inversion which (a) simulates seismic waves by solving the seismic wave equation (Fichtner et al., 2006a, 2006b; Tape et al., 2007; Tromp et al., 2005), (b) iteratively improves numerical models using the adjoint-state method (Tarantola, 1984), and (c) in seismology, has historically focused efforts on inverting for short-period ($T > 2$ s) earthquake-generated surface waves (e.g., Fichtner et al., 2010; Krischer et al., 2015; Tao et al., 2018; Tape et al., 2010; Zhu et al., 2015). By solving the seismic wave equation, adjoint tomography honors the intrinsic physics of wave propagation, overcoming limitations inherent in ray theory (e.g., Montelli et al., 2004). The transition to full-waveform techniques has been accelerated by the development of efficient numerical solvers that accurately simulate seismic wave propagation (e.g., Komatitsch et al., 2002), and automated workflow tools which reduce the algorithmic complexity involved in large-scale inversions (e.g., Chow et al., 2020; Krischer et al., 2015; Modrak et al., 2018). Typical resolutions in earthquake-based adjoint tomography are limited to long-wavelength crustal and mantle structure (e.g., Bozdağ et al., 2016; Chen et al., 2015; Fichtner et al., 2010; Krischer et al., 2018; Tao et al., 2018; Zhu et al., 2015), or crustal structure in regional settings with sufficient seismicity and station coverage (Miyoshi et al., 2017; Tape et al., 2010).

New Zealand is characterized by high levels of seismicity, a permanent seismic network, and an existing regional 3D tomography model. In Chow et al. (2020) we demonstrated the feasibility of applying full-waveform tomography to the North Island of New Zealand through data–synthetic misfit assessment and realistic synthetic inversions. Building upon this work, we undertake the first application of adjoint tomography in New Zealand to generate and interpret a high-resolution velocity model of the Hikurangi subduction zone and the North Island of New Zealand. The main goals of this study are to:

1. Perform earthquake-based adjoint tomography for the North Island;
2. Assess the updated velocity model based on waveform improvement, velocity changes, and point spread functions;
3. Identify and interpret the most striking velocity changes.

The paper begins with an overview of the tectonic setting (Section 2). An explanation of methodologies (Section 3) is followed by a description of data used in the inversion (Section 4). Section 5 presents the final velocity model alongside an accompanying resolution analysis (Section 6). The paper closes with a discussion of the most striking velocity changes (Section 7). A companion paper (Chow et al., 2022) provides a more detailed look at three specific velocity changes in the Hikurangi subduction wedge, and their interpretations. In this paper we focus on interpretations of velocity changes in North Island basement terranes, Taupō Volcanic Zone, and Cook Strait.

2. Tectonic Setting

The Hikurangi subduction zone is a convergent plate boundary where the Pacific plate subducts westward beneath the Australian plate at a rate of ~40 mm/yr (Barnes et al., 2010; Collot et al., 1996; DeMets et al., 1994; Lewis & Pettinga, 1993; Nicol et al., 2007). The margin exhibits substantial along-strike differences in structure and interseismic coupling (Barnes et al., 2010; Wallace et al., 2004, 2009). In the area of Figure 1, the subducting Pacific plate mostly comprises the Hikurangi Plateau, a Cretaceous large igneous province (Mortimer & Parkinson, 1996; Taylor, 2006) that is considerably thicker than the subducting oceanic crust further north

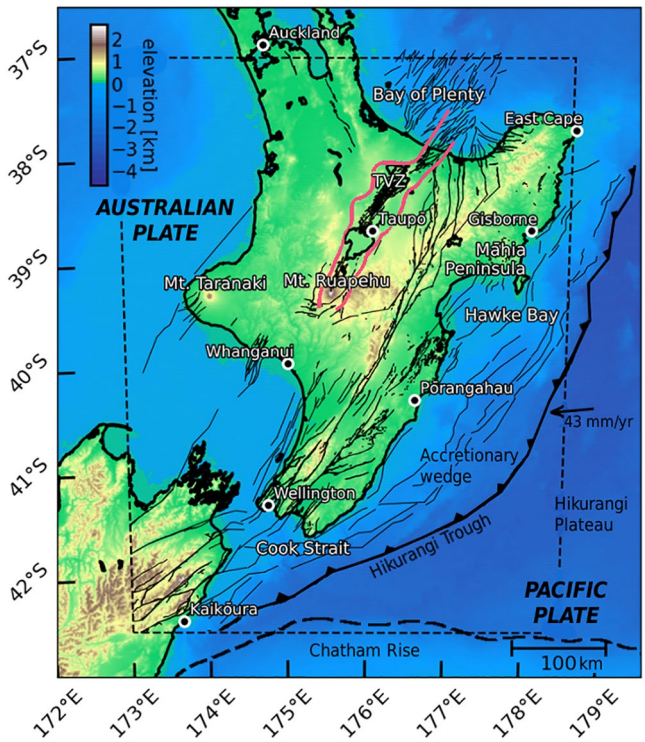

Figure 1. Tectonic setting for the North Island of New Zealand. New Zealand active onshore and offshore faults plotted as thin black lines (Litchfield et al., 2014). The thick, dashed, black line shows the continent-ocean boundary between the Chatham Rise and the Hikurangi Plateau. Elevation values are defined by SRTM-30P (Becker et al., 2009), which are also used to define topography and bathymetry for the numerical mesh. Geographic and tectonic landmarks are labeled, with select towns and cities marked by black circles. The solid red lines show the outline of the Taupō Volcanic Zone (TVZ). The tomographic simulation domain is shown by the thin, dashed, black outline.

(Davy et al., 2008; Mochizuki et al., 2019). In the southern part of Figure 1, the Pacific plate consists of the thick (~23–26 km) continental crust of the Chatham Rise (Eberhart-Phillips & Reyners, 1997; Reyners et al., 2017). Due to its composition, much of the Hikurangi forearc above the shallow part of the plate interface is exposed sub-aerially due to buoyancy of the subducting plate (Litchfield et al., 2007; Nicol et al., 2007), resulting in a significantly shallower dip angle of the Pacific plate slab with respect to the adjacent Kermadec and Tonga subduction margins (Jarrard, 1986). The Hikurangi trench is consequently closer to the coastline—between 40 and 120 km (Figure 1)—in comparison with typical subduction settings (e.g., Cascadia, Nankai, Northern Japan). The plate interface below land is located at ~15 km depth below the east coast of the North Island (Figure 2; Williams et al., 2013).

New Zealand is commonly divided into lithologically distinct basement terranes that are separated by faults or melanges and overprinted by more recent tectonic processes (Edbrooke et al., 2015; Mortimer, 2004). In the North Island, a system of left-lateral strike-slip faults along the eastern edge of the island accommodates ~6 mm/yr of the total convergence in the north and ~20 mm/yr in the south (Nicol & Beavan, 2003). In the central North Island, the active magmatic arc is represented by calderas and volcanoes of the Taupō Volcanic Zone (TVZ). The TVZ is also a zone of active extension characterized by high heat flow and geothermal activity, extensional faulting, and corresponding seismicity (Wilson et al., 1995, 2009). The maximum rate of extension in the TVZ is 20 mm/yr (Villamor & Berryman, 2006). Further west, volcanism occurs at Mt. Taranaki, which is unusual in both its location and eruptive composition (Sherburn et al., 2006; Sherburn & White, 2006). Offshore of the west coast of the North Island are two large sedimentary basins, the Taranaki basin (e.g., King & Thrasher, 1996) and Whanganui basin (Carter & Naish, 1998). The Hikurangi subduction margin terminates below the northern South Island, where plate convergence becomes dominantly strike-slip along the Alpine fault (e.g., Sutherland et al., 2007; Wallace et al., 2007), after a complex transition from oblique subduction to oblique transpression in Cook Strait and through the Marlborough fault system (e.g., Eberhart-Phillips & Bannister, 2010; Pondard & Barnes, 2010; Reyners et al., 2017).

Seismic activity associated with the Hikurangi subduction zone is frequent and varied in terms of faulting mechanism and location (Ristau, 2008; Townend et al., 2012). Subduction seismicity is characterized by intraplate events within the subducting Pacific plate and interplate seismicity along the megathrust subduction interface. In the upper plate, seismicity is observed as extensional faulting of the central North Island (Darby et al., 2000; Villamor et al., 2017), and left-lateral strike-slip faulting along the length of the margin (Nicol & Beavan, 2003). In the northern South Island, the 2016 M_w7.8 Kaikōura earthquake ruptured many distinct faults (Hamling et al., 2017; Holden et al., 2017) and produced an extensive aftershock sequence (Chamberlain et al., 2021; Lanza et al., 2019). To the north, the 1947 M_w7.0 Gisborne earthquakes generated some of the largest tsunamis in New Zealand history (Bell et al., 2014) and exhibited many of the characteristics of "tsunami earthquakes" defined by Kanamori (1972).

Geodetic observations have been used to observe slow slip events (SSEs) and determine slip rate deficit along the Hikurangi plate interface (Wallace, Beavan, et al., 2012; Wallace, 2020). At the northern margin, SSEs have been observed offshore and close to the trench, where the plate interface is shallow at depths of 5–15 km (Wallace, 2020). In contrast, at the southern Hikurangi margin the plate interface is inferred to be locked to roughly 30 km depth, with SSEs observed at depths of 30–45 km (Wallace, Beavan, et al., 2012; Wallace, 2020). Wallace et al. (2009) proposed that if the geodetically locked southern portion of the Hikurangi margin were to slip seismically, it would be capable of producing a megathrust event as large as M_w ~ 8.2–8.7.

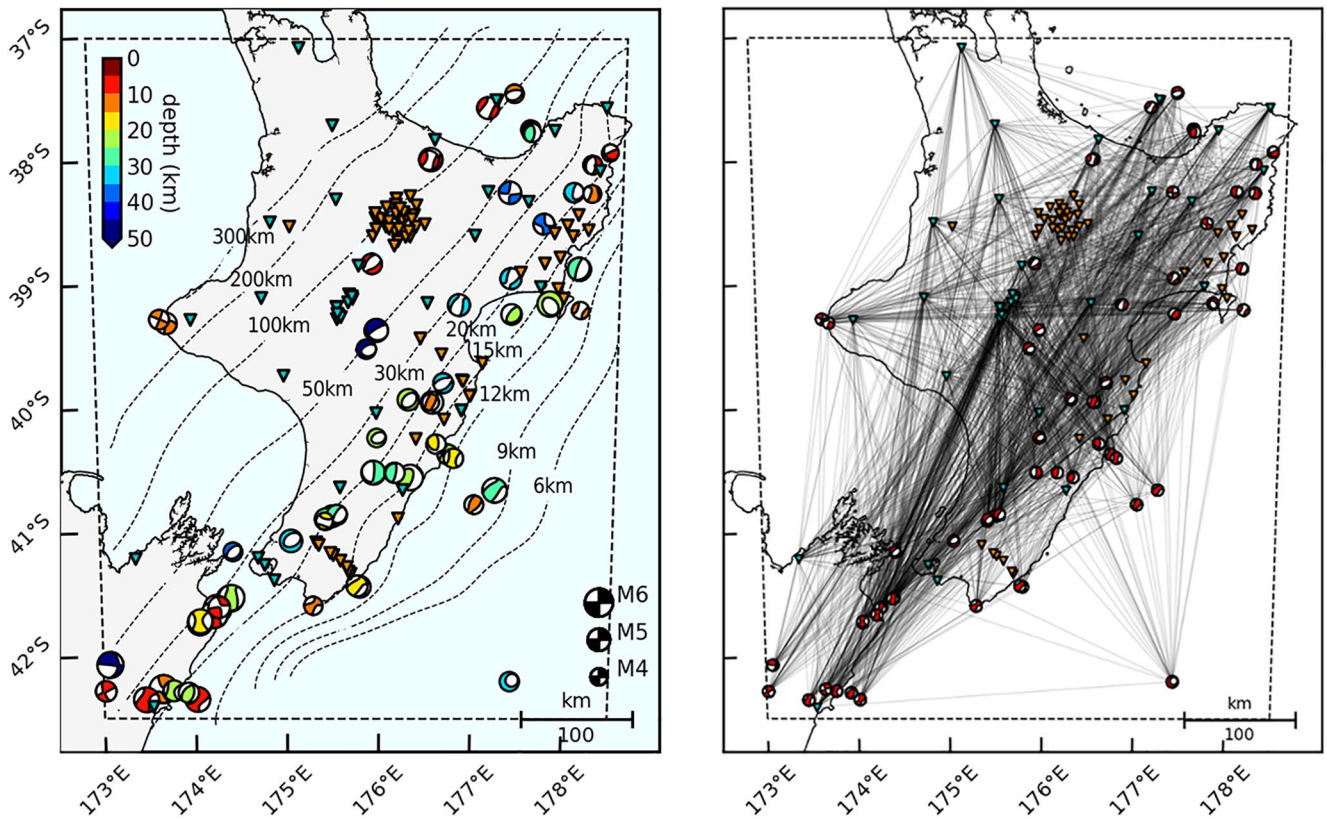

Figure 2. Sources and receivers included in the inversion. Left: 60 earthquakes shown as focal mechanisms, color coded by depth, and scaled by magnitude. 88 broadband seismic stations shown as inverted triangles, with 38 permanent network (GeoNet) stations colored blue, and 50 temporary network stations colored orange. Plate interface model of Williams et al. (2013) shown as dashed contour lines. Right: Source–receiver ray paths for the first iteration of the inversion. Sources and receivers same as in left panel. Connecting raypaths only shown for sources and receivers that have at least one measurement window.

3. Methods

Adjoint tomography seeks to minimize data–synthetic waveform misfit through iterative improvements of model parameters that represent sources and structure. In this study we undertake adjoint tomography using regional earthquakes following the methodologies outlined in Chow et al. (2020).

3.1. Forward Modeling and Misfit Function

The forward problem solves the seismic wave equation, given representations of an earthquake and Earth structure. For forward simulations we use the time-domain spectral element solver, SPECFEM3D Cartesian (Komatitsch et al., 2005; Komatitsch & Tromp, 2002a, 2002b). To mesh the North Island, we use hexahedral elements and a rectangular domain with roughly 450 km by 600 km horizontal extent and 400 km vertical extent. Topography and bathymetry are explicitly honored at 1 km spacing interpolated from SRTM-30P elevations (Becker et al., 2009). Elevations at the top of the mesh range ±3 km, and no water layer is included. Because the minimum required element size decreases with depth, we include two coarsening layers in the mesh. At each coarsening layer, the horizontal element spacing doubles and vertical element spacing triples.

To avoid unnecessary computational expense in the early iterations, we use two mesh resolutions. For the initial long-period iterations, we use a coarse mesh with minimum element spacing of 2 km at the surface that is accurate down to 8 s. For later iterations, when the minimum waveform period falls below 8 s, we use a fine resolution mesh with minimum element spacing of 1 km. The fine-resolution mesh is accurate to 2.5 s period. The coarse- and fine-resolution meshes contain 88,000 and 220,000 elements, respectively.

The misfit between observed (data) and simulated (synthetic) seismograms is quantified for each component (north, east, up) using a windowed cross-correlation traveltime misfit function (CC). Our choice of CC over other misfit functions is primarily motivated by our automated workflow tool, which forgoes careful inspection of waveforms. We also consider phase-based misfit functions, which have been shown to extract more information from waveforms over more traditional methods like CC (Bozdağ et al., 2011; Yuan et al., 2020). However, these misfit functions also require more careful application to deal with issues arising from noisy data, cycle-skipping (instantaneous phase; Bozdağ et al., 2011), and loss of misfit function convexity for large phase differences (exponentiated phase; Yuan et al., 2020). Similarly, in Chow et al. (2020), we extensively tested CC against the multitaper misfit function for the North Island domain. This previous experience, alongside the fact that both misfit functions exhibited similar behavior, further motivates our use of CC.

All simulations are run for 300 s, starting 20 s prior to the earthquake origin time. To selectively restrict data included in the inversion, an automatic time-windowing algorithm is applied (Maggi et al., 2009), which ignores undesirable signals such as low signal-to-noise ratio observations. Within a given time window i, the misfit function is defined as

$$\chi_i(\mathbf{m}) = \frac{1}{2}\left[\frac{T_i^{obs} - T_i(\mathbf{m})}{\sigma_i}\right]^2, \tag{1}$$

where T^{obs} is the observed traveltime, $T(\mathbf{m})$ is the corresponding synthetic traveltime for a model $\mathbf{m}$, and σ is a measurement uncertainty weight (Tromp et al., 2005). For each iteration, misfit defined by Equation 1 is averaged over all windows for a given event, and for all events in a given iteration. The objective function for a given model $\mathbf{m}$ is defined as

$$F(\mathbf{m}) = \frac{1}{2S}\sum_{s=1}^{S}\frac{1}{N_s}\sum_{i=1}^{N_s}\chi_i(\mathbf{m}), \tag{2}$$

where S is the total number of sources, and N_s is the total number of windows for a given source s (Tape et al., 2010). Equation 2 is used as a measure for overall data–synthetic misfit for a given velocity model.

3.2. Inverse Problem

The inverse problem seeks to iteratively improve the Earth model by minimizing the misfit function $F(\mathbf{m})$ (Equation 2). For each iterative model update, we first compute the gradient of the misfit function using the adjoint-state method (Fichtner et al., 2006a; Tape et al., 2007; Tarantola, 1984; Tromp et al., 2005). The L-BFGS optimization algorithm provides a search direction using a low-rank quadratic approximation to the objective function (Nocedal & Wright, 2006). The algorithm provides convergence properties of second-order optimization methods, while avoiding the significant expense of full Hessian computation or assembly. We determine step length along the search direction using a backtracking line search (Chow et al., 2020; Modrak & Tromp, 2016).

Our velocity model is defined by P- and S-wave velocity (V_p, V_s), density, and attenuation (Q_p, Q_s). At each iteration, derivatives with respect to V_p and V_s are computed using the adjoint-state method, and only V_p and V_s are updated. Density is held constant due to its limited sensitivity to the surface wave measurements primarily used (Nazarian & Stokoe, 1984). Attenuation is also held constant since the misfit function depends on phase but not amplitude (Equation 1). Following Chow et al. (2020), we carefully select events from a reviewed catalog. We do not perform source inversions to update hypocenters or moment tensors because the regional moment tensor solutions derived by GeoNet fit regional long-period waveforms and are consistent with Global CMT solutions and New Zealand tectonics (Ristau, 2008, 2013). In addition, our tomographic inversion will down-weight minor, random errors in source mechanism through averaging with other events.

Regularization is often used in tomographic inversions to suppress nonuniqueness (Modrak & Tromp, 2016). In this work we smooth the gradient by convolution with a 3D Gaussian to suppress poorly constrained small-scale components of the updated models. Horizontal and vertical half-widths are chosen larger than the expected spatial resolution of input data to promote resolution of large-scale features in early iterations. Waveform bandpass and gradient smoothing length are reduced gradually throughout the inversion to conservatively approach the global minimum of the objective function (Figure 3).

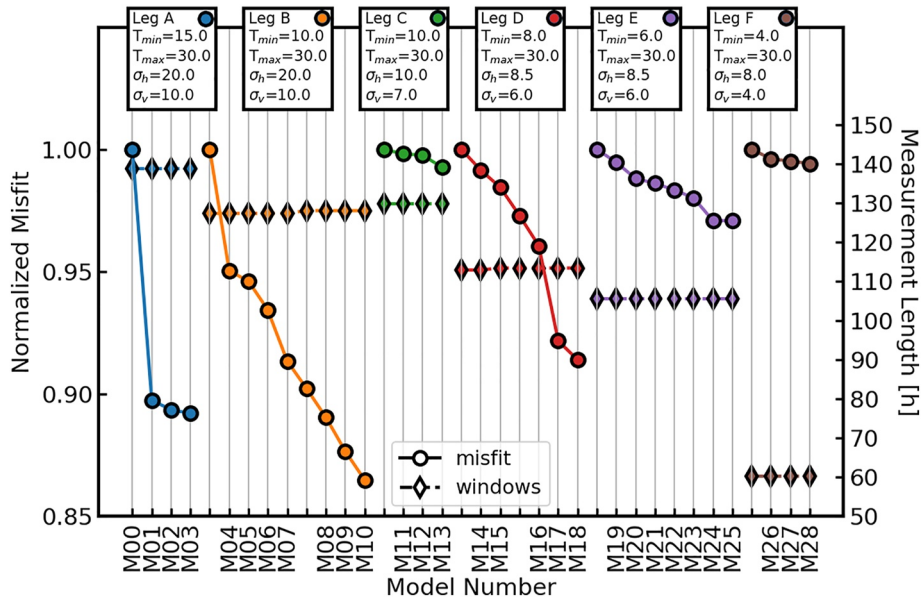

Figure 3. Convergence plot which shows reduction of waveform misfit over the course of the inversion. Each colored line represents an individual inversion leg. Bandpass ($T_{\min}$, $T_{\max}$) and horizontal and vertical standard deviations of the 3D Gaussian used for gradient smoothing (σ_h, σ_v) are annotated above each leg. Misfit (Equation 2) is plotted as circles and normalized to the starting misfit of each given inversion leg. Diamonds show cumulative window length in hours. Adjacent points that share a model number (e.g., at the transition between inversion legs) correspond to re-evaluation of the misfit using the same model, for example, through re-selection of time windows using new windowing parameters, or through a change of the listed parameters ($T_{\min}$, $T_{\max}$, σ_h, σ_v).

4. Data

4.1. Study Area and Starting Model

With the North Island of New Zealand as our study area, domain edges are chosen based on source and receiver locations as well as computational expense (Figure 2). Regions north of Auckland (37°S) were excluded due to limited station coverage and a lack of large magnitude ($M_w > 4$), shallow (depth > 60 km) events. The eastern boundary (178.5°E) is limited to the sub-aerial extent of the North Island, chosen to minimize the amount of deep-ocean model space with little data coverage. The southern (42.5°S) and western (173°E) boundaries are chosen to include a number of aftershocks and related seismicity from the 2016 M_w7.8 Kaikōura earthquake (Hamling et al., 2017; Holden et al., 2017). In this work all locations are converted to, and shown in, the UTM 60S coordinate system.

The starting velocity model is defined by the NZ-Wide2.2 velocity model of Eberhart-Phillips, Bannister, Reyners, et al. (2020). This velocity model was developed using ray-based traveltime tomography with body waves and surface waves (Eberhart-Phillips & Fry, 2017, 2018). This 3D velocity model defines V_p, V_p/V_s, density, and attenuation (Q_p, Q_s; Eberhart-Phillips et al., 2015; Eberhart-Phillips et al., 2017; Eberhart-Phillips, Bannister, & Reyners, 2020) for the entire New Zealand region. Our starting V_s model is created through direct division of the NZ-Wide2.2 V_p and V_p/V_s models. In Chow et al. (2020) we assessed waveform misfits for 250 regional earthquakes using this starting velocity model and showed that data–synthetic time shifts for >25,000 measurements are reasonable for adjoint tomography.

4.2. Earthquake Sources

We select 60 regional earthquakes with high signal-to-noise ratio waveforms recorded between 2004 and 2019 (Figure 2; Table S1). In the target bandpass of 4–30 s, surface waves are the dominant signals. Event magnitudes are $4.5 \leq M_w < 6.0$ with depths less than 60 km. In general, waveforms from events with $M_w < 4.5$ are recorded by only several stations in the network, limiting their usefulness at the regional scale. Events with $M_w \geq 6.0$ are also excluded because our simulations use point source approximations, while large magnitude events may require

finite fault solutions for accurate synthetic waveforms. Moment tensors in New Zealand are routinely calculated by GeoNet (Ristau, 2008) using the Time Domain Moment Tensor algorithm (Dreger, 2003), and are available for regional earthquakes since 2003.

Although the initial catalog of suitable events contains ~250 events, a large number of these are foreshock and aftershock sequences, which densely cluster certain regions of the domain with spatially and mechanistically similar earthquakes. These events produce near-identical waveforms at the period range of interest (4–30 s), and without any explicit weighting considerations (e.g., Ruan et al., 2019), repeated contributions from such source–receiver paths are observed to have an undesired effect on the inversion. Stacked contributions from these paths mask out more unique source–receiver paths during the inversion, leading to anomalously strong contributions in regions with dense event clustering.

To optimize our selection of events, we perform event declustering by gridding the model domain into 10 × 10 horizontal bins and two vertical sheets (depths of 0–20 km and 20–200 km), totaling 200 grid cells. We specify that only two events from the initial catalog can be retained per grid cell, leading to more uniform coverage throughout the domain and a preferential selection of crustal (<20 km) events. Events recorded on temporary stations are also prioritized to ensure unique receiver locations are included. We choose a final catalog size of 60 events to maximize the number of unique event locations without including too many similar locations or moment tensors (Figure 2). From the remaining catalog we select 60 additional events with the same magnitude and depth range as a validation catalog for later model assessment (Section 5.4).

4.3. Receivers

Three-component broadband seismic data are collected for 88 stations from permanent and temporary networks (Figure 2; Table S1). The permanent seismic network of New Zealand is operated by GeoNet (https://www.geonet.org.nz/), with 38 broadband stations included within the study area. Data from an additional 50 broadband stations are included. In total, 1,800 unique source–receiver paths are used (Figure 2), with temporary network data providing roughly 8% of the initial data set.

Temporary seismometer deployments throughout the North Island are used to enhance coverage of the permanent network. For our study, we deployed the Broadband EAst COast Network (BEACON) in southern Hawke's Bay (Kaneko & Chow, 2017). BEACON consisted of 22 broadband, three-component station locations which recorded for 1.5 years between 2017 and 2019 (Text S1 in Supporting Information S1). In the southern North Island, the Seismic Analysis of the HiKurangi Experiment (SAHKE) transect consisted of a line of broadband and short-period seismic receivers deployed perpendicular to the trench to capture offshore shots and image plate interface characteristics (Henrys et al., 2013). Our data set includes broadband data from the SAHKE line, as well as two deployments focused on the Taupō Volcanic Zone (Bannister, 2009) and the Gisborne region (Figure 2; Table S2; Bannister & Bourguignon, 2011).

5. Results

Here we present the results of our inversion and the final velocity model (M28; Figure 4). Model differences with respect to the initial model (M00) are shown in terms of net model update $\ln(M_{28}/M_{00})$, which to first order approximates the percentage difference ($M_{28}/M_{00} - 1$) but more reliably represents model differences over a wide range of values with respect to the percentage difference (Tape et al., 2007).

Heterogeneous velocity changes are recovered best in V_s, so we primarily discuss V_s and V_p/V_s structures in the following sections. We also address waveform improvement for select source–receiver pairs (Figure 8) and in total (Figure 9).

5.1. Inversion Legs

We perform 28 L-BFGS iterations over six distinct inversion legs (Figure 3). The start of each inversion leg is defined by selection of new time windows and a change of input parameters including some or all of: waveform bandpass, windowing algorithm parameters, smoothing length for the full, volumetric gradient of the misfit function.

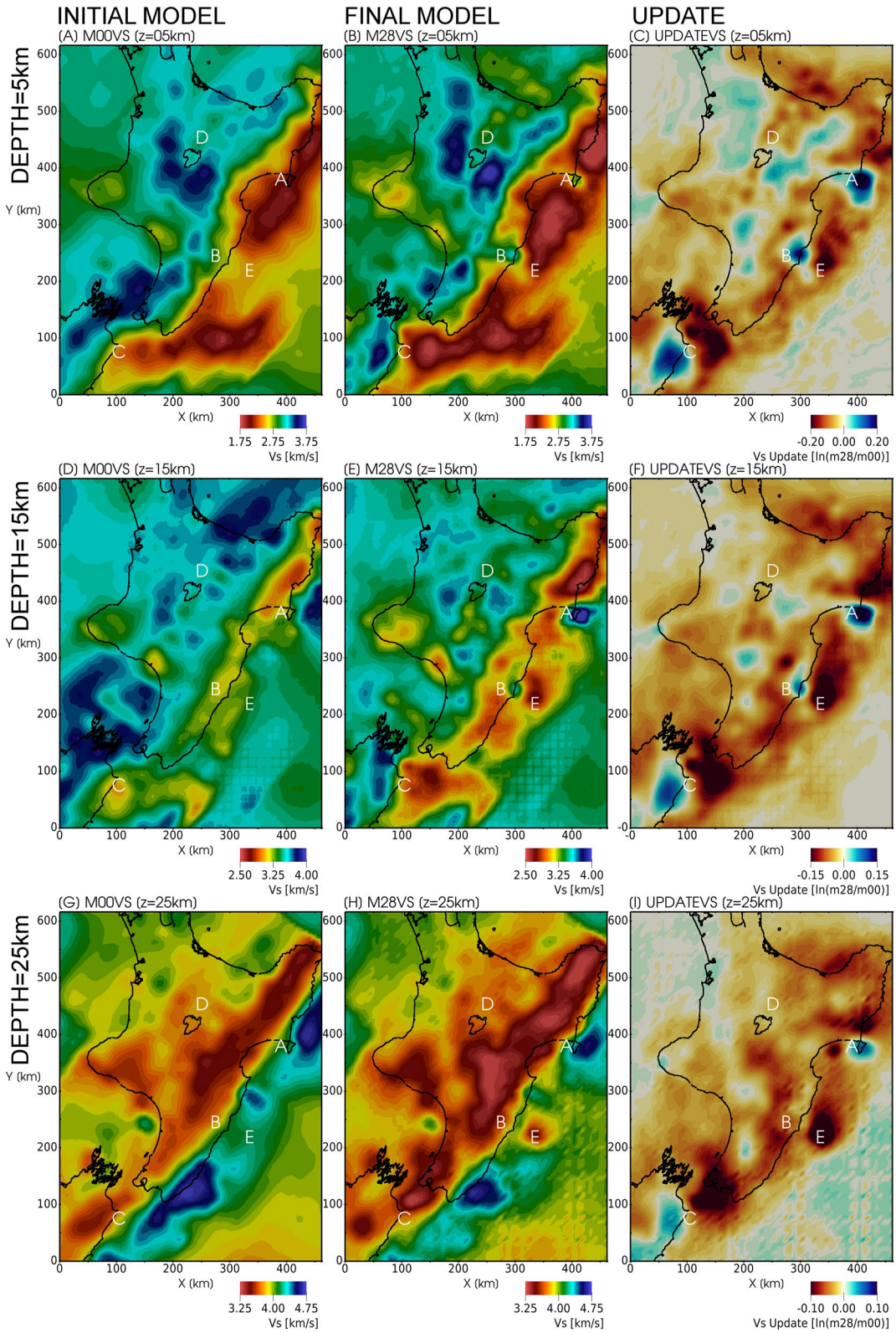

Figure 4. Comparisons of initial (M00) and final (M28) V_s velocity models at various depth slices. Columns represent initial model (M00; left), final model (M28; center), and net model update (ln(M28/M00); right). Rows represent depth slices at 5 km (top), 15 km (middle), and 25 km (bottom). Annotated letters A–E relate to notable features discussed in Section 5. Note the differing color scales between rows and columns. Numerical artifacts related to mesh coarsening layers (Section 5.1) are visible in panels (d, e, f, h, and i).

To help ensure convergence to the global minimum, we progress from low to high frequencies over the course of the inversion (e.g., Akcelik et al., 2003; Bunks et al., 1995; Fichtner et al., 2009; Krischer et al., 2018; Tape et al., 2010). New time windows are chosen at the beginning of each leg, and remain mostly fixed throughout a given leg to ensure that misfit assessment compares a similar segment of the data set. Time windowing parameters are modified slightly at each leg to reflect changes in input parameters.

The choice to begin a new inversion leg was in some cases motivated by the behavior of the nonlinear optimization algorithm. Loss of descent direction, negligible misfit reduction, or a large number of step counts in the line search (>5) can be indicators of convergence within a given passband. In such cases, we discard the accumulated L-BFGS history and move on to a new leg. However, because restarting the nonlinear optimization is computationally expensive, we discard L-BFGS history only when signs of numerical stagnation, like those above, are present. At the start of each leg, multiple trial iterations are performed to determine a suitable set of windowing parameters, waveform bandpass, and smoothing length. Characteristics for an acceptable suite of parameters include similar misfit and number of measurements as the previous iteration.

Mesh resolution was changed between inversion legs D and E (Figure 3) to accommodate higher frequency waveforms. This method saved roughly 400,000 CPU-hours by allowing the initial four inversion legs to be performed on a low-resolution mesh. However, due to the dissimilar mesh constructions, the change required interpolation between regular and irregular grids. As a result, mesh artifacts are visible at depths corresponding to coarsening layers of the coarse mesh (e.g., Figure 4e). These artifacts are only visible in regions with little to no resolution (e.g., southeast of the Hikurangi trench); they do not affect waveform propagation simulations and therefore do not impact our interpretations.

5.2. Velocity Changes

The final velocity model shows large, heterogeneous velocity changes with respect to initial values within the 3D model (Figure 4). The maximum net model update values are +0.33 for V_s (Figure 5) and +0.25 for V_p (Figure 6). The most striking heterogeneities are visible at mid-crustal depths (15 km; Figures 4d–4f) which taper off by 25 km (Figures 4g–4j). In general, the final model is characterized by slower wavespeeds, with specific areas requiring substantial positive velocity changes. Most of the changes do not introduce new features, but rather serve to modify existing velocity features through changes in wavespeed, as well as sharpening and shifting of existing velocity gradients (Figure 4).

Moderate-sized (>50 km) shallow (<5 km) features like the low-velocity accretionary wedge, the high-velocity axial mountain ranges, and the low-velocity Taranaki and Whanganui basins (Figure 1) are identifiable in both initial and final models (Figures 4a and 4b). These similarities are expected since the longest waveform period of 30 s corresponds to spatial resolutions less than 100 km, for an average V_s of 3 km/s. On average, velocity changes range in values from 5%–20% in the upper 30 km, with velocity changes of at least 1% above 75 km depth. By 100 km depth the two models are the same due to the limited depth sensitivity of 30 s surface waves. At 25 km depth (Figure 4i), large (>50 km) features are characterized by the plate interface region, with the high-velocity Pacific plate contrasting the slower relative velocities of the upper Australian plate. As expected, in regions with sparse data coverage (i.e., deep ocean, offshore the west coast of the North Island), velocity changes are negligible.

Consecutive net model updates at 5 km depth (Figures 5 and 6) show the final iteration of each inversion leg (Figure 3). In V_s, initial resolution of long-wavelength (>100 km) structure (Figure 5a) is gradually improved with increasing detail (Figures 5b–5f). The most striking velocity features (labels A–E), are already visible by the second inversion leg (Figure 5b), suggesting that they were necessary to fit the initial long-period waveforms. The last two inversion legs (Figures 5e and 5f) mainly serve to sharpen existing features and increase detail. Consecutive V_p updates follow a similar trend as V_s (Figure 6), although the amplitude of change is less, probably because the initial ray-based model was derived primarily using *P*-wave direct arrivals.

Crustal heterogeneity at 5 km depth is visually dominated by three, strong, (> 20%), positive velocity changes, labeled A, B, and C in Figure 4. These perturbations introduce positive velocity anomalies in the forearc region, visible directly beneath (A) Māhia Peninsula, (B) Pōrangahau, and (C) the northern South Island. Adjacent to the positive velocity anomaly Feature C is a low-velocity perturbation offshore (e.g., Figures 4b and 4c). Together

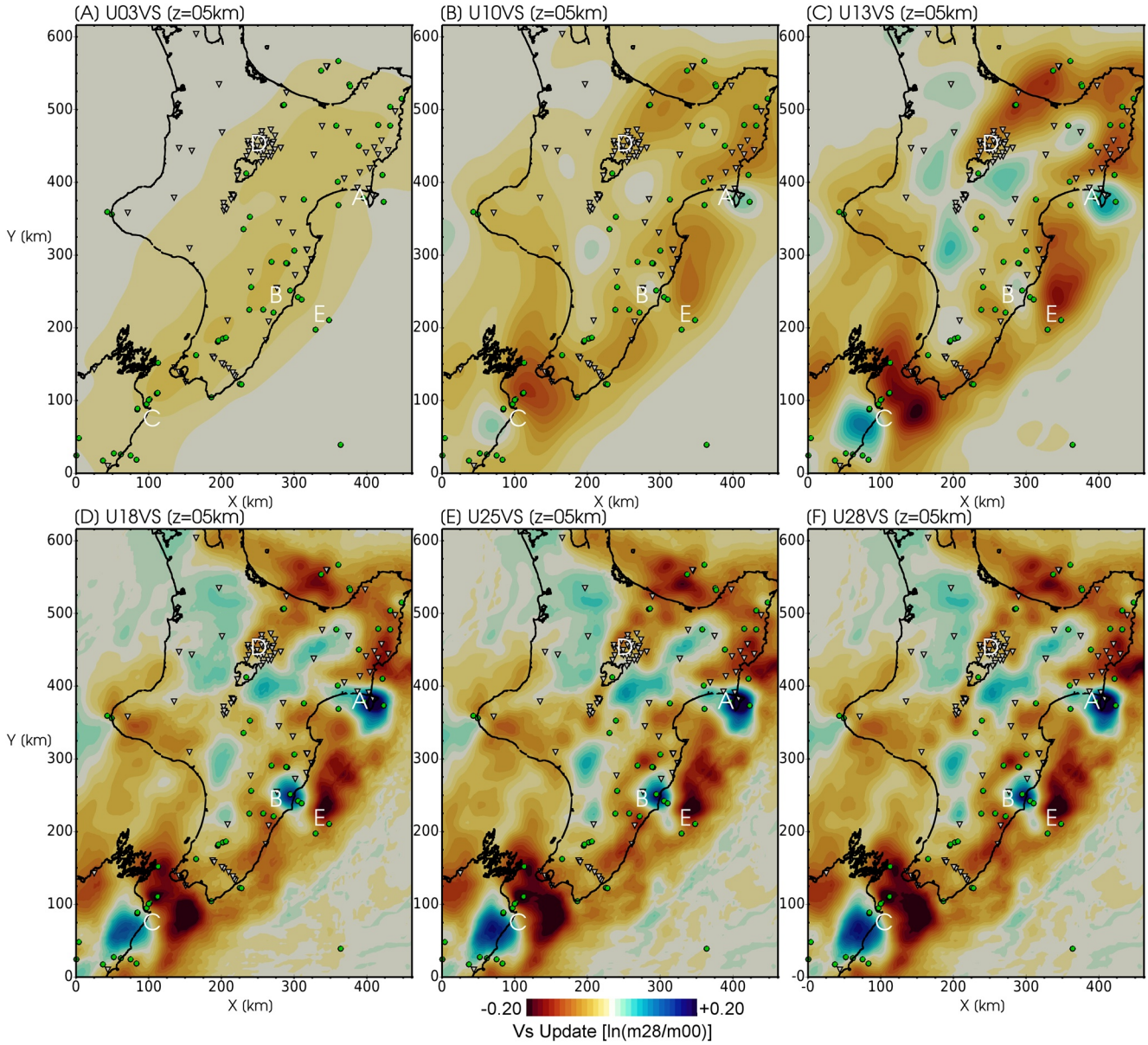

Figure 5. V_s net model updates at 5 km depth for the final iteration of each inversion leg (Figure 3). Features A–E are the same as in Figure 4. The color scale is the same for each figure, at ±0.20, or approximately ±20% velocity change. Note that the color scale saturates, and maximum velocity changes by M28 are as much as ±30%. Source locations are depicted by green dots; station locations are depicted by inverted triangles.

these velocity changes image a strong velocity gradient in the transition from the South Island to Cook Strait. In the central North Island, at 5 km depth, slow velocities in the TVZ (feature D) are bounded by high velocities to the east and west (Figure 4b). This strong gradient is most prominent at 5 km depth (Figure 4b) and is no longer visible by 25 km depth (Figure 4h). Offshore Pōrangahau, feature E highlights a localized, negative velocity change which is most visible as a strong low-velocity anomaly at 25 km depth (Figures 4h and 4i).

The ratio of seismic velocities (V_p/V_s) is often used in tomographic studies in conjunction with interpretations of absolute velocity; high V_p/V_s has been inferred to correlate with increased clay content in sedimentary rocks, increased porosity, highly fractured rocks, and increased fluid pressures (e.g., Audet et al., 2009; Christensen, 1996; Eberhart-Phillips et al., 2005, 1989; Ito et al., 1979). With increased sensitivity to V_s structure from our surface waves measurements, we see strong changes in the M28 V_p/V_s model, shown at 5 km depth in Figure 7.

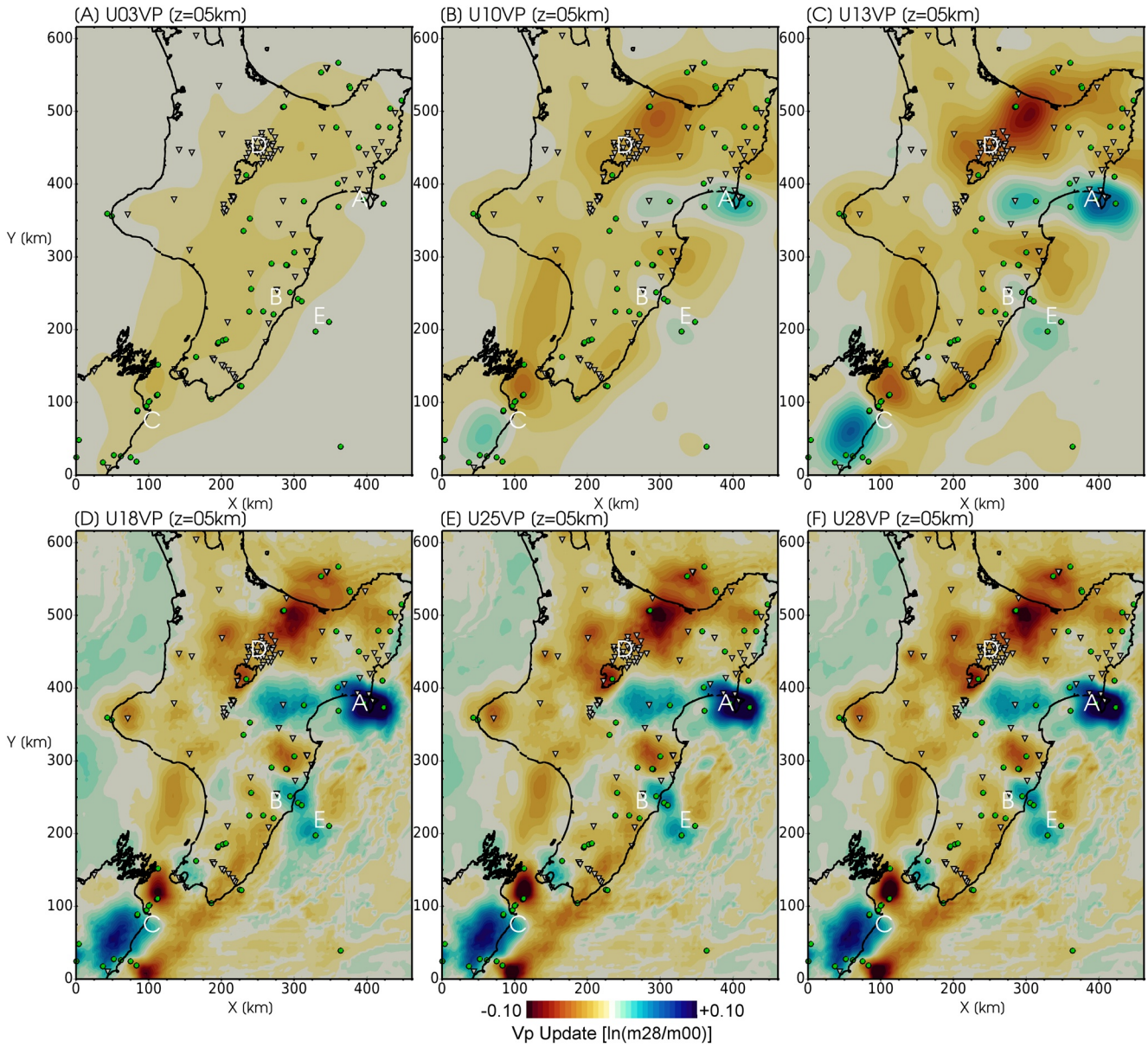

Figure 6. V_p net model updates at 5 km depth for the final iteration of each inversion leg (Figure 3). Features A–E are the same as in Figure 4. The color scale is the same for each figure, at ±0.10, or approximately ±10% velocity change. Note that the color scale saturates, and maximum velocity changes by M28 are as much as ±25%. Source locations are depicted by green dots; station locations are depicted by inverted triangles.

Our V_p/V_s model is derived through direct division of the M28 V_p and V_s models, which can be susceptible to apparent structures arising due to resolution differences of the respective models. We caution over-interpreting V_p/V_s in regions where the model updates show varying levels of resolution (Figures 5 and 6) and focus our subsequent interpretations on long-wavelength (> 50 km) V_p/V_s structures. We also note that the net model updates of V_s (Figure 4c) and V_p/V_s ratio (Figure 7c) show strong similarities, suggesting that the resolved differences in V_p/V_s are predominately related to changes in V_s structure.

5.3. Waveform Improvement

Waveforms show considerable improvement from the initial (M00) to final (M28) velocity models, but data–synthetic misfits still remain by M28 (Figure 8). Here we discuss waveforms at 6–30 s to emphasize longer-period

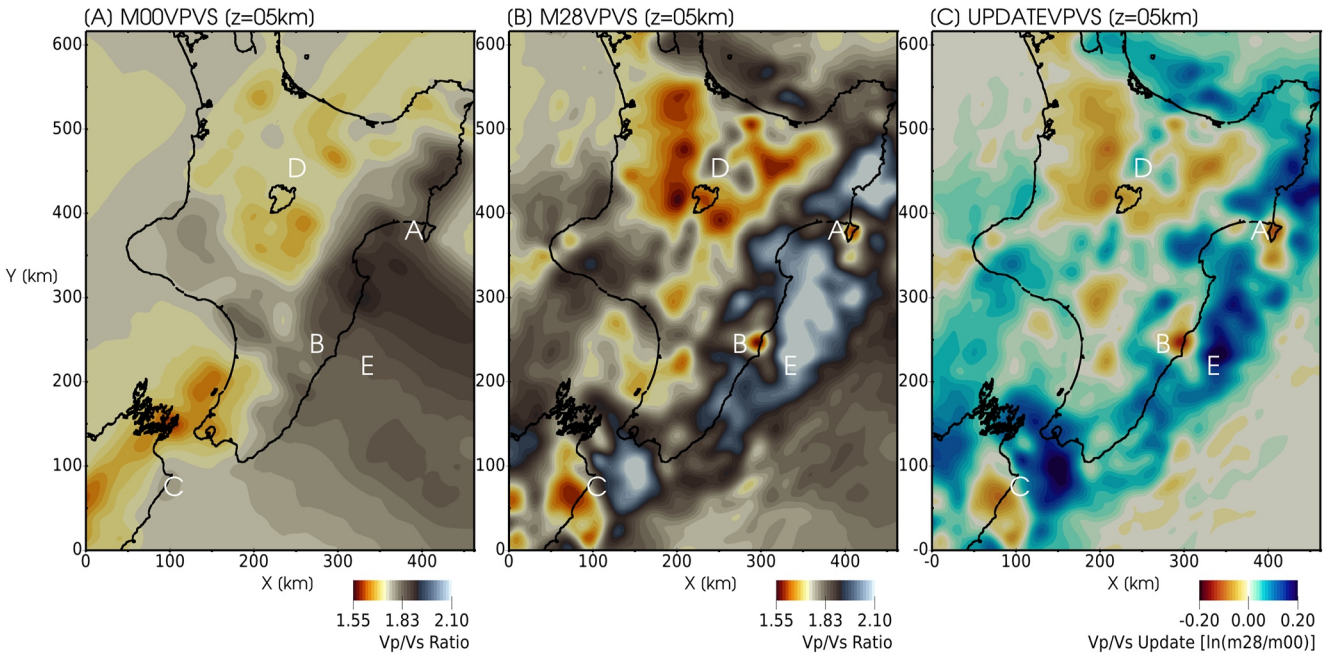

Figure 7. Comparisons of V_p/V_s ratio at 5 km depth. The V_p/V_s ratio for a Poisson's solid ($V_p/V_s = 1.73$) corresponds to white colors. (a) Initial model (M00) at 5 km depth. (b) Final model (M28) at 5 km depth. (c) Net model update ln(M28/M00) at 5 km depth. Labels A–E relate to features discussed in Section 5 and shown in Figure 4.

surface wave signals, because waveforms at 4–30 s begin to show lower signal-to-noise ratios and are therefore less illustrative of waveform improvement.

Data–synthetic misfit is compared in Figure 8 for eight representative source–receiver pairs. Misfit windows selected for the initial and final models are shown in orange. One of the benefits of the automated windowing procedure is that we do not need to explicitly pick phases, which is emphasized by the variation in misfit window start time and length for different source–receiver pairs (Figure 8). To get an idea about the sections of the seismic wavefield included in our inversion, we create a traveltime plot of measurement start times vs. source–receiver distances and calculate apparent velocities (Figure A1). The apparent velocities from both the initial and final models suggest that the measurements are predominantly long-period (>4 s) direct arrivals and surface waves, but are also likely to contain more complex seismic phases (Figures A1b and A1d). Including such a medley of seismic phases provides additional sensitivity to structure compared to more classical body-wave tomography, as well as confidence that our data set is sensitive to both V_p and V_s structure.

The waveforms in Figure 8 show that direct (P) arrivals are well fit by the initial model, which is to be expected from a tomography model derived from body-wave traveltimes (e.g., Figure 8a). Surface waves and later arrivals in the initial model show considerable time shift with respect to the data at this bandpass (e.g., Figures 8b and 8c). Paths which pass through relatively simple crustal structure (e.g., Figures 8e–8h) show better initial waveform fit with respect to raypaths that travel near or through more complex tectonic regions such as the low-velocity accretionary wedge (e.g., Figures 8b–8d). The large initial misfit of an offshore source (Figure 8d) shows the limited accuracy of the initial model away from land.

After the inversion, long-period (>10 s) time shifts are reduced to <1 s and surface waves for all waveform shown are better fit, although high-frequency components show varying degrees of misfit (Figure 8e). Some synthetics—both in M00 and M28—show high-frequency components not seen in data (Figure 8c). Amplitude information, which is not inverted for, shows little to no improvement, and in most cases data–synthetic amplitude differences do not change (Figure 8c). Errors in high frequencies and amplitudes might be attributable to inaccuracies in the underlying attenuation model at short periods, since it is not updated during the inversion. Similarly, coda waves are left mostly unimproved (e.g., Figure 8d), hinting at the difficulty of accurately resolving small-scale heterogeneities and basin effects caused by sharp impedance contrasts (e.g., Kaneko et al., 2019).

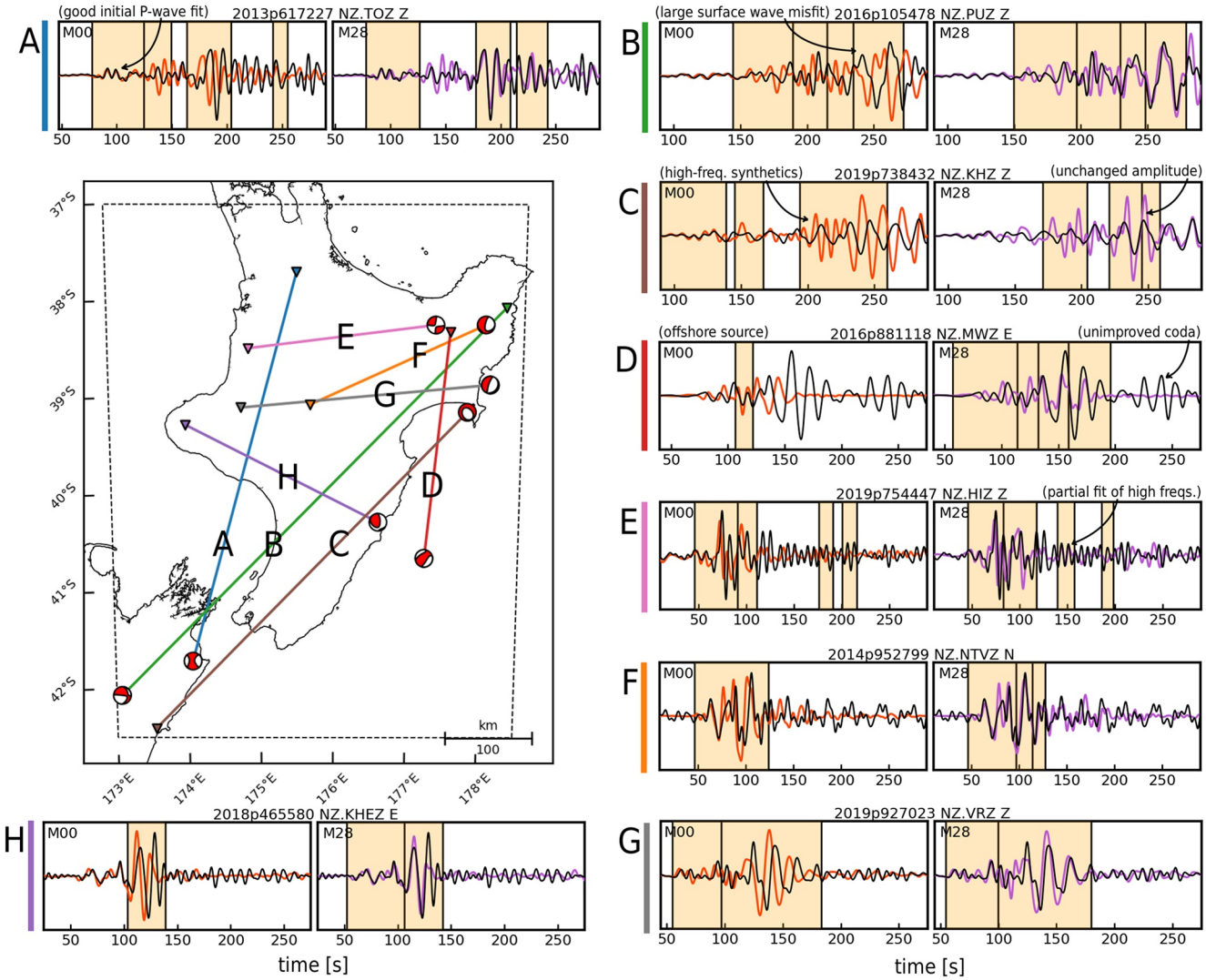

Figure 8. Waveform comparisons for eight unique source–receiver pairs. Each comparison (A–H) consists of two panels showing data (black) and synthetics for the initial model (M00; red) and final model (M28; purple), and their respective misfit windows (orange). All waveforms are processed and filtered identically within a bandpass of 6–30 s. The map shows corresponding moment tensors, receiver locations, and raypaths. GeoNet earthquake event ID, station code, and waveform component are annotated in the title of each panel. Select waveforms are annotated based on corresponding text in Section 5.3, with freq. as a shorthand for frequency. Waveforms are shown in units of displacement [m].

5.4. Bulk Misfit Assessment

Total normalized misfit (Equation 2) is reduced over the 28 iterations (Figure 3). The largest (>10%) relative reductions in misfit occur in the initial long-period inversion legs, A and B (Figure 3). Total seismogram window length is also maximum here at 500,000 s or 138 hr. At Leg C, an attempt to reduce gradient smoothing while retaining bandpass was made. The negligible misfit reduction suggests that the previous inversion leg B was capable of fitting the 10–30 s period range (Figure 3). At 8–30 s (Leg D) another large decrease in overall misfit occurs. By 6–30 s (Leg E) the behavior of the misfit reduction is less pronounced than earlier inversion legs (Figure 3).

For later inversion legs (E, F), signal-to-noise ratio increased as the waveform bandpass included more high-frequency noise signals such as the secondary microseism (5–10 s; Webb, 1998). This is noted in the large decrease in total measurements for the 4–30 s period band (Figure 3). Total measurement length here is roughly 60 hr, less than half of the initial inversion legs. After the final model, a number of trial iterations were run on an ultra-fine resolution mesh using 3–30 s waveforms. At these shorter periods, observed waveform signal-to-noise ratio

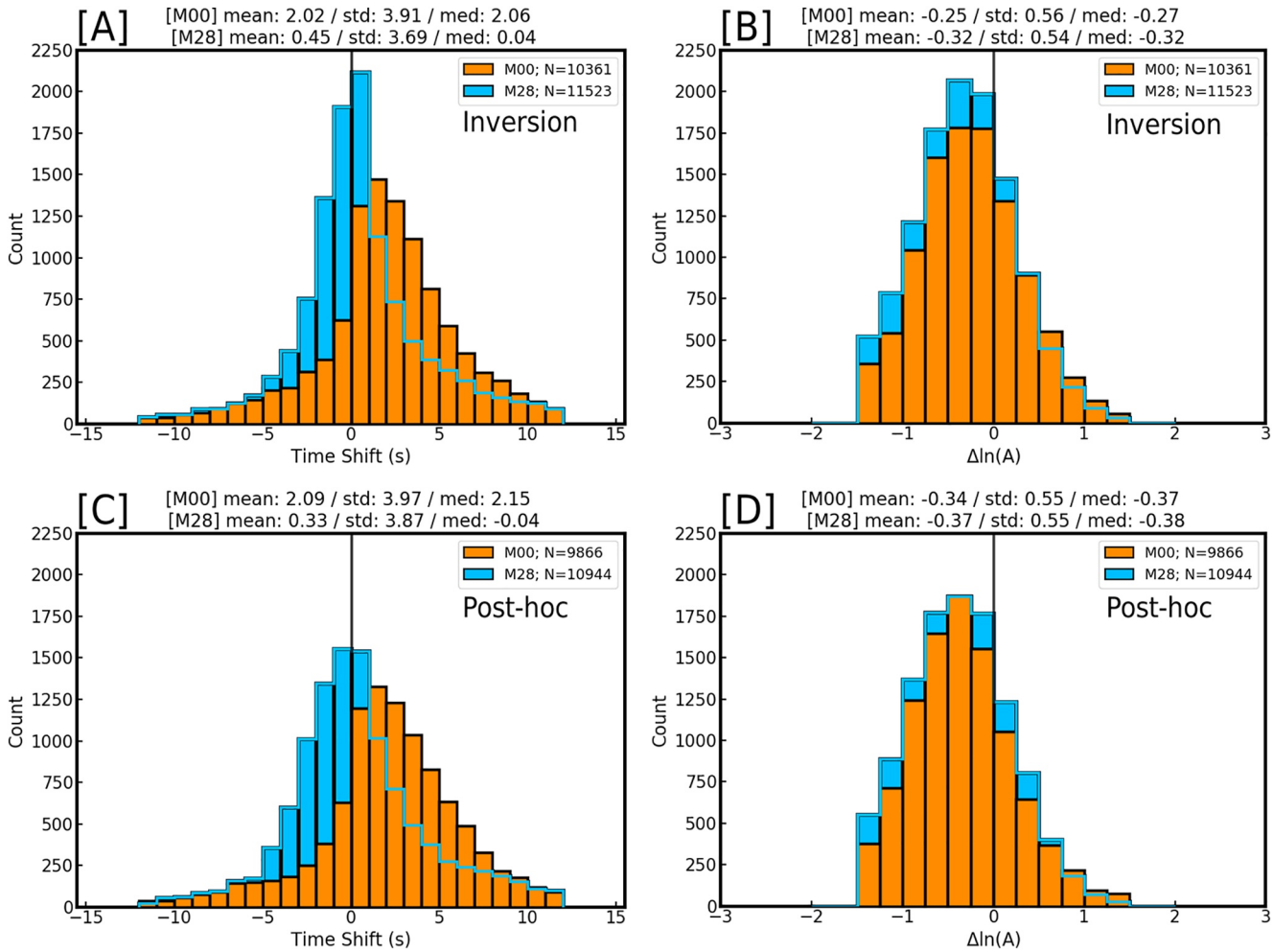

Figure 9. Misfit histograms detailing bulk misfit assessment between the initial model (M00; orange), and final model (M28; blue) for 60 events used in the inversion (top) and a separate 60 event post-hoc validation catalog (bottom). All histograms are based on 6–30 s waveforms. Mean, standard deviation, and median values for each respective histogram are given in the title of each figure. The number of measurements for each histogram is provided in the respective legends. Amplitude difference is defined as $\Delta \ln A = \ln\left[\int d^2(t)dt / \int s^2(t)dt\right]$, where d and s are observed and synthetic waveforms. (a) Time shift for inversion events. (b) Amplitude difference for inversion events. (c) Time shift for post-hoc events. (d) Amplitude difference for post-hoc events.

increased further and misfit reduction was negligible with respect to previous inversion legs. At this point, we decided to terminate the inversion.

Histograms are a useful method for showing time shifts and amplitude differences in bulk (Figure 9). Amplitude differences here are defined as $\Delta \ln A = \ln\left[\int d^2(t)dt / \int s^2(t)dt\right]$, where d and s are observed and synthetic waveforms, respectively (Dahlen et al., 2000). Bulk misfit assessment for 6–30 s is performed for the initial and final models using the 60 inversion events (Figures 9a and 9b) and 60 separate post-hoc events (Figures 9c and 9d). The inversion time shift histogram shows that the initial time shift of 2.0 ± 3.9 s is reduced to 0.5 ± 3.7 s by the final model (Figure 9a). Amplitude differences show negligible change between initial and final models, which is expected since we use a phase-only misfit function (Figures 9b and 9d). The post-hoc histograms show similar behavior to the inversion results (Figures 9c and 9d), suggesting that the overall velocity changes have resolved meaningful structure, evidenced by improvement of data not included in the inversion.

Misfit reduction is largest in Legs A, B, and D of the inversion, with a range of approximately 10%–15% misfit reduction (Figure 3). To get an idea of how normalized misfit reduction translates to overall time shift, we can do a back-of-the-envelope calculation. Values for Equation 2 taken from Figure 9a give an average time shift of $\chi(\mathbf{m}) = 2\ s$, for a total of $S = 60$ events, with $i = 167$ measurements per event ($N \approx 10{,}000$ measurements). For these values we recover $F(\mathrm{m}) = 1$. If our inversion improves 25% of our measurements by 1 s (i.e., $\Delta T = 1$ s), we

get $F(\mathrm{m}) = 0.875$, or a 12.5% misfit reduction. We would expect the same normalized misfit ($F(\mathrm{m}) = 0.875$) if we improved all of our measurements by $\Delta T = 0.25$ s. This helps illustrate that misfit reduction (Figure 8) is likely a mix of: a small percentage of large time shifts (e.g., large surface wave time shift in Figure 8b) and a large number of small time shifts (e.g., small direct arrival time shifts in Figure 8f).

5.5. Computational Expense

The total inversion required approximately 500,000 CPU-hours on the New Zealand eScience Infrastructure's high performance computer, named Māui. Forward simulations require 0.5 hr on 40 cores for the coarse-resolution mesh, and 0.75 hr on 80 cores for the fine-resolution mesh. For each iteration, 60 forward simulations and 60 adjoint simulations are performed to generate synthetics and gradient, respectively. Gradient smoothing occurs once per iteration at the cost of approximately one forward simulation. Waveform preprocessing and misfit quantification are run in serial, and totaled roughly 2,000 CPU-hours for the entire inversion.

An additional $60 \times N$ forward simulations are required for the line search to find an acceptable step length that suitably reduces the objective function. If the L-BFGS search directions are well scaled, then only one line search step should be required (Modrak & Tromp, 2016). In practice, N ranged between 1 and 3 for each iteration. If N reached values greater than 5, a new inversion leg was started.

6. Resolution Analysis

Resolution information is important for assessing tomographic inversions, particularly when the velocity models are used for interpretations of Earth structure and tectonic processes. However, exhaustive tomographic model assessment techniques are computationally infeasible with large, heterogeneous velocity models (e.g., Nolet, 2008; Tarantola, 2005). One method for resolution testing in full waveform tomography is the point spread function (Fichtner & Trampert, 2011b), which has been used in previous adjoint tomography studies (e.g., Bozdağ et al., 2016; Tao et al., 2018; Zhu et al., 2015).

Point spread functions (PSF) are a measure of how much a point-localized perturbation is smeared, or blurred, by the inversion procedure. Fichtner and Trampert (2011b) showed that the action of the Hessian on a model perturbation $\mathbf{H}(\mathbf{m})\delta\mathbf{m}$ can be viewed as a conservative estimate of the PSF, providing practical information on the extent to which features in a tomographic model can be interpreted. In practice we calculate PSFs using a finite-difference approximation

$$\mathbf{H}(\mathbf{m})\delta\mathbf{m} \approx \mathbf{g}(\mathbf{m} + \delta\mathbf{m}) - \mathbf{g}(\mathbf{m}), \tag{3}$$

where $\mathbf{H}(\boldsymbol{m})$ denotes the Hessian evaluated at the final model $\mathbf{m}$, $\mathbf{g}(\boldsymbol{m})$ the gradient evaluated at the final model, and $\delta\mathbf{m}$ is a local model perturbation with respect to the final model.

We denote PSFs in the form H_{XY}, where X defines the quantity in which the perturbation is made (V_p or V_s), and Y denotes the quantity defining the recovered point spread function. For example, H_{SS} refers to a V_s point spread function for a perturbation in V_s, whereas H_{PS} quantifies parameter trade-offs, and shows the effect of a V_p perturbation on V_s recovery.

6.1. Individual Point Spread Functions

To probe the resolution of individual features in our velocity model, we define a perturbation at a discrete point in the model and recover $\delta\mathbf{m}$ using Equation 3. The motivation for each point-localized perturbation is to probe the robustness of features in terms of size, shape, and location. We define perturbations as 3D Gaussians with different horizontal (σ_{h}) and vertical half-widths (σ_z). The full-width of the Gaussian is defined as $\Gamma = \sqrt{8}\sigma$. Since we are investigating V_s velocity anomalies, perturbation are made in V_s with peak amplitudes equal to $\pm$15% of background M28 V_s model values. We place these perturbations at various locations around the model, corresponding to the prominent velocity features (A–E) discussed in Section 5. The results for features B and C are discussed in Section 7 alongside tectonic interpretations. The point spread functions for features A, B, and E are discussed in detail in Chow et al. (2022).

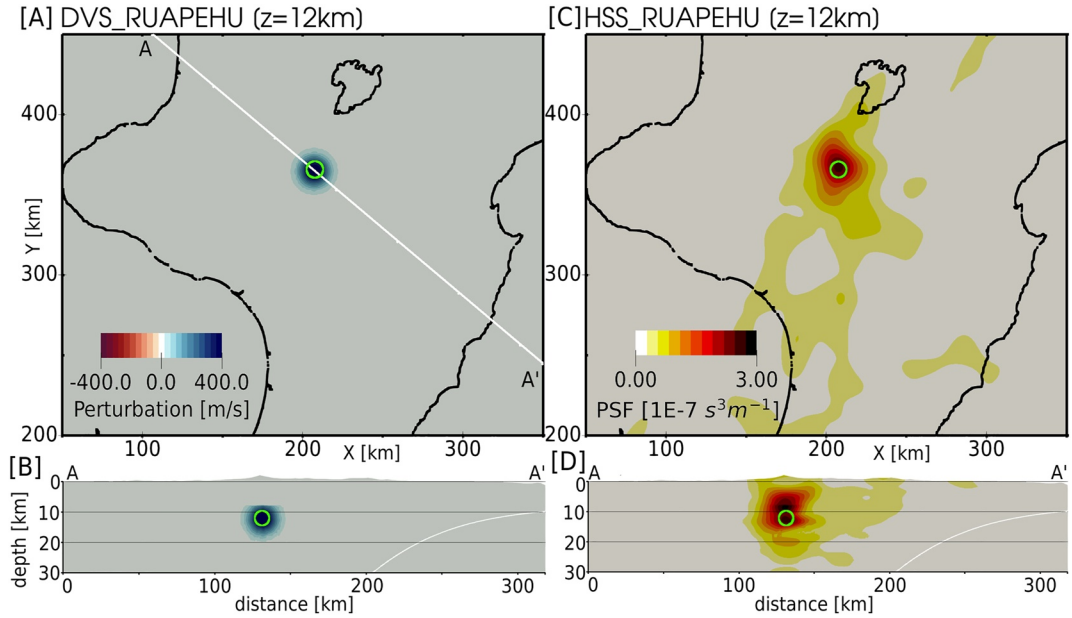

Figure 10. An example point spread function (PSF). (a), (b) 3D spherical Gaussian velocity perturbation placed at 12 km depth. The peak amplitude of the perturbation is 15% of the final V_s velocity model. The horizontal and vertical full-widths of the perturbation (green circles) are 10 and 5 km, respectively. (c), (d) Recovered PSF illustrating how the perturbation is smeared by the inversion procedure. A–A' cross sections are shown at 2x vertical exaggeration. White lines in cross sections correspond to the plate interface model of Williams et al. (2013).

One example of a point spread test is shown in Figure 10. The positive-velocity perturbation is defined at 12 km depth below the central North Island, with horizontal and vertical full-width of 10 and 5 km, respectively (green circles; Figures 10a and 10b). The peak amplitude of the Gaussian is 15% of the final V_s velocity model or approximately 400 m/s. We apply this perturbation to the final M28 V_s model and calculate $\mathbf{g}(\mathbf{m} + \delta\mathbf{m})$ in the same manner as Section 3 to recover the PSF (Equation 3). As in the inversion, we apply regularization to this gradient to suppress unwanted small-scale components.

The resultant PSF (Figures 10c and 10d) shows acceptable recovery of the central peak (dark colors; Figure 10c), but in cross-section the peak is smeared ~5 km above the input location (Figure 10d), suggesting some uncertainty in recovering its exact depth. Outside of the full-width of the Gaussian, where perturbation amplitudes fall below 5% of the final V_s velocity model, lateral smearing of about 1.5–2 times the size of the actual perturbation (Figures 10a and 10b) is visible in both the horizontal and vertical directions (orange–red colors; Figures 10c and 10d). This is likely due to regularization and limited resolution of the data set to such low-amplitude perturbations. The lowest-amplitude region of the PSF (yellow colors; Figures 10c and 10d) shows patches to the north and south, suggesting that limited constraint of the data set in these regions will result in minor velocity changes far from the responsible anomaly.

6.2. Zeroth Moment Test

For insight into how resolution varies not just for individual features, but across the entire model, we evaluate the action of the Hessian on a constant volumetric V_s perturbation $\delta\mathbf{m} = 50$ m/s using Equation 3. The result, shown in Figure 11, is equal to the Fourier transform of the Hessian at zero wavenumber, or the zeroth moment (Fichtner & Trampert, 2011a).

Similar to the ray-coverage plot in Figure 2b, the zeroth order moment test provides information about how resolution varies in a relative sense throughout the model, but does not measure resolution length directly. In the case of uniform volumetric data coverage, full recovery of the volumetric perturbation might be possible. In practice, however, significant departure from full recovery results from the limited sensitivity of the data set to structure outside the source–receiver configuration. Slices through the recovered zeroth order moment are shown in Figure 11. A threshold value is chosen manually to outline a volume in which velocity changes may be interpreted.

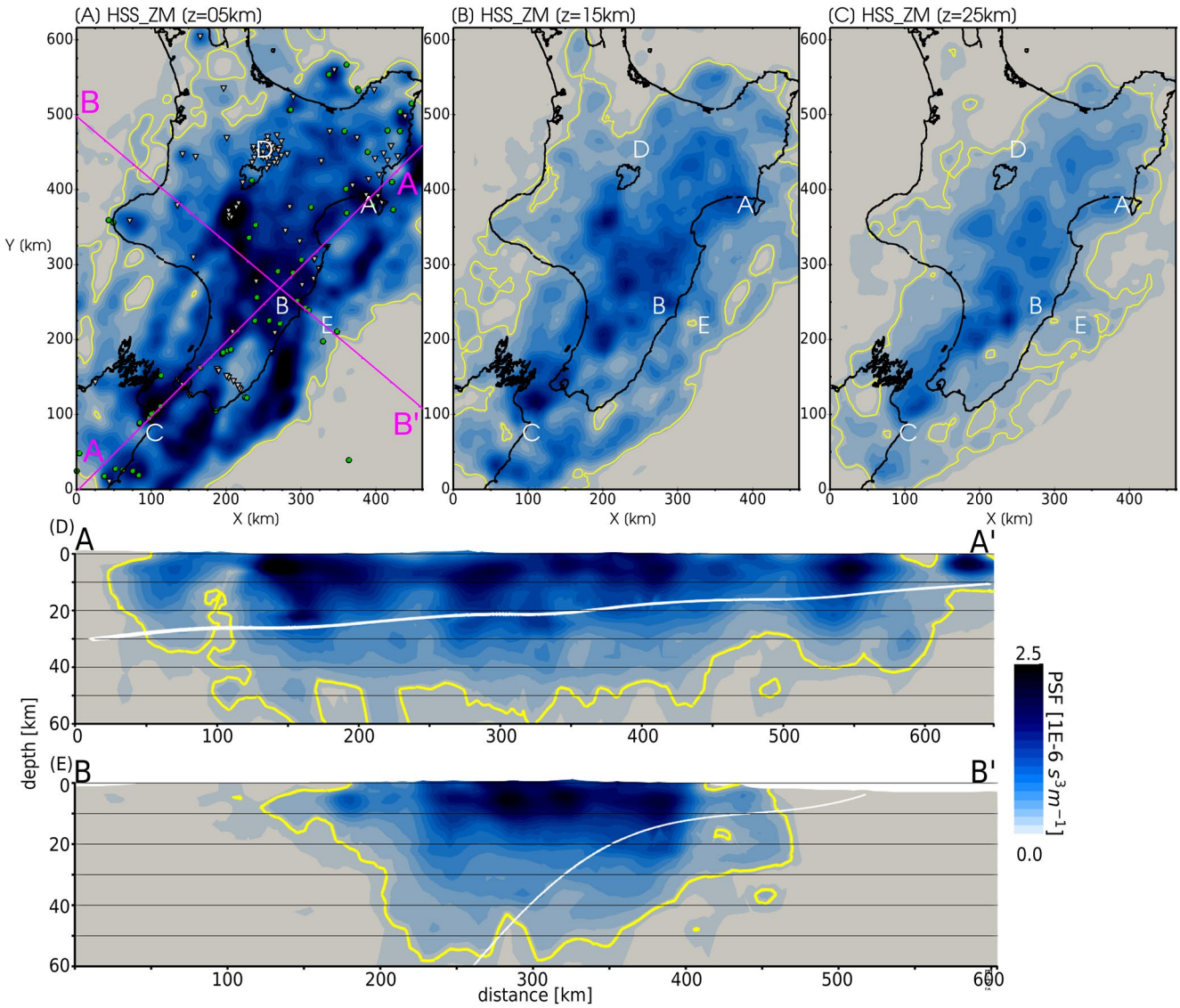

Figure 11. Zeroth moment test showing relative weight of point spread functions for a homogeneous 50 m/s V_s perturbation with respect to the final velocity model. The volumetric field approximates the sensitivity of the entire set of waveform measurements to perturbations in V_s structures. Solid yellow lines outline a threshold value of 2.5×10^{-7} s^3 m^{-1}. (a) H_{SS} at 5 km depth. Pink lines show surface traces of cross sections in (d) and (e). Earthquakes and receivers used in inversion are depicted as green circles and white inverted triangles. (b) H_{SS} at 15 km depth. (c) H_{SS} at 25 km depth. (d) H_{SS} A–A' cross section to 60 km depth at 2x vertical exaggeration. (e) H_{SS} B–B' cross section. White lines in cross sections correspond to the plate interface model of Williams et al. (2013).

The largest relative amplitudes of the zeroth moment are found in the top 10–15 km (Figures 11a, 11d and 11e), reflecting the dominant influence of surface waves in our data set. Interestingly, these surface waves traveling through the low-velocity accretionary wedge and forearc basins extend sensitivity of land-based measurements 50–100 km offshore (Figures 11a and 11b). With increasing depth, the lateral extent of the zeroth moment shrinks. By 25 km depth, sensitivity is primarily limited to below land (Figures 11c). Vertical cross sections reveal that the data set is sensitive to structure down to 50 km, however the strongest relative sensitivity is limited to the top 20–30 km (Figures 11d and 11e). Based on the zeroth moment coverage, we confine our interpretations to the upper 30 km.

7. Discussion

7.1. Comparisons With Geology and Tectonics

The structure of our updated velocity model has several points of comparison with the known geologic basement terranes of New Zealand and their sedimentary and volcanic cover (Figure 12a; Mortimer, 2004; Edbrooke et al., 2015). In this section we make comparisons between geology and our updated V_s model, and note that V_p and V_p/V_s structures follow similar trends as V_s (Figures 12c and 12d).

Regional-scale (100 s km) shallow velocity structures are broadly controlled by the contrast between the exposed basement terranes to the west ($V_s > 2.5$ km/s), and the low-velocity forearc basin and accretionary wedge to the east ($V_s < 2$ km/s; Figures 12a and 12b). The boundary between these two tectonic features lies inland of the East Coast and spatially correlates with the axial ranges separating the volcanic arc and forearc basins, as well as the Esk Head Melange separating the Kaweka and Pahau/Waioeka terranes (black dashed line, Figure 12a). In V_p/V_s this boundary is less defined but spatially similar. The juxtaposition of high V_p/V_s (> 2) in the forearc region against low V_p/V_s (< 1.8) to the west may be the boundary between lower-velocity, fluid-saturated forearc sediments and exposed basement rocks of the upper plate (Figure 12c). Visible in both V_s and V_p/V_s along this boundary are shallow, upper-plate expressions of the two high-velocity, low-V_p/V_s anomalies identified as features A and B in Section 5. These are discussed in detail in Chow et al. (2022).

Moderate-sized features (~50 km) correspond well to basement terranes and individual tectonic features around the North Island. High velocities ($V_s > 3$ km/s; Figure 12b) and moderate to low V_p/V_s (< 1.8; Figure 12c) below the central North Island striking northeast–southwest show good agreement with the Waioeka, Kaweka, and Rakaia greywacke and schist terranes (Figure 12a). In the northeast near East Cape, a notch of high velocities ($V_s > 2.5$ km/s; Figure 12b) shows similar shape to the boundary between the Pahau terrane and the East Coast Allochthon, a body of tectonically displaced sedimentary and volcanic rock. West of the TVZ, high velocities ($V_s > 3.5$ km/s) extend northward, spatially correlating with the western boundary of the Morrinsville terrane (Figure 12a). Corresponding high velocities are not seen in V_p (Figure 12d), potentially due to more limited V_p resolution in this region. In the northern South Island, the Caples terrane is overprinted by high-velocity schist, and has previously been associated with a distinct patch of high V_p (Eberhart-Phillips et al., 2005). V_s structures show a patch of high velocity ($V_s \approx 3$ km/s) extending offshore, generally coinciding with the offshore extent of the Caples terrane (Figure 12b).

Other velocity structures can be related to non-basement geologic features of the North and South Islands. In the TVZ, low velocity ($V_s < 2.5$ km/s) and high V_p/V_s (> 1.8) extending from Ruapehu northwest into the Bay of Plenty (Figure 12b) are likely related to magmatic processes in the active volcanic arc. At shallow depth (3 km), we image a wide, low-velocity, high-V_p/V_s, zone spatially correlated with the TVZ (Figure 12). Embedded within this low-velocity zone are ovular patches of low-V_s ($V_s < 2.5$ km/s) (Figure 12b). We also image patches of low-V_p ($V_p < 4.5$ km/s) offset from these V_s anomalies (Figure 12d), which leads to heterogeneous V_p/V_s structure throughout this volcanic region (Figure 12c). Along the west coast of the North Island, patches of low velocity crust are likely associated with the rubbly, low-porosity ring plain of Taranaki Volcano and with low-velocity sediments in the Taranaki and Whanganui Basins (Figure 12a). In the southern end of the study area, strong velocity gradients separate high velocity ($V_s > 3$ km/s) of the North and South Islands with low velocities ($V_s < 2$ km/s) in Cook Strait (Section 7.3).

Comparisons with two geologic cross sections along the East Coast show shallow (<10 km) vertical resolutions at the scale of kilometers (Figure 13). In the two examples crossing through northern Hawke's Bay (Figures 13c and 13e) and central Hawke's Bay (Figures 13d and 13f), the final V_s model shows low velocity layers agreeing with the geometry of the 20–30 km-scale faulted anticlines and synclines that extend from the surface down to ~10 km depth. These features are visible at both Northern and Central Hawke's Bay, providing a link between V_s structure and geologic observations of crustal structure, deposition age, and sedimentary composition (Francis et al., 2004). Feature A (Figure 4) is also visible at depth in northern Hawke's Bay (Figure 13e), and is discussed in further detail in Chow et al. (2022).

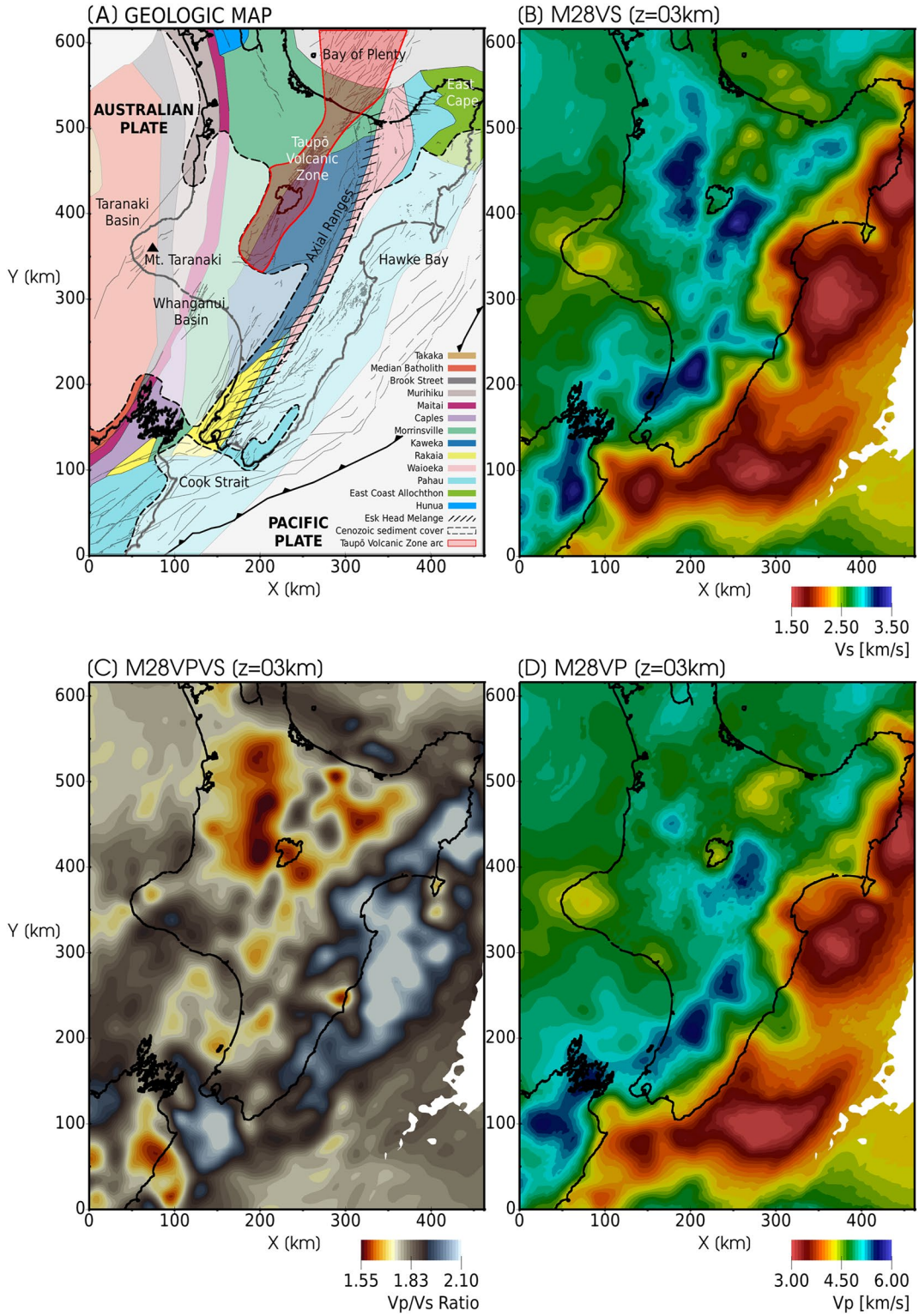

Figure 12. A comparison of New Zealand geology (Edbrooke et al., 2015; Mortimer, 2004) and the final velocity models (M28) at 3 km depth. (a) Thin gray lines show active faults (Litchfield et al., 2014). (b) M28 V_s. (c) M28 V_p/V_s. (d) M28 V_p. The white region on the right side of the velocity models corresponds to bathymetry deeper than 3 km, and therefore no velocity values are available.

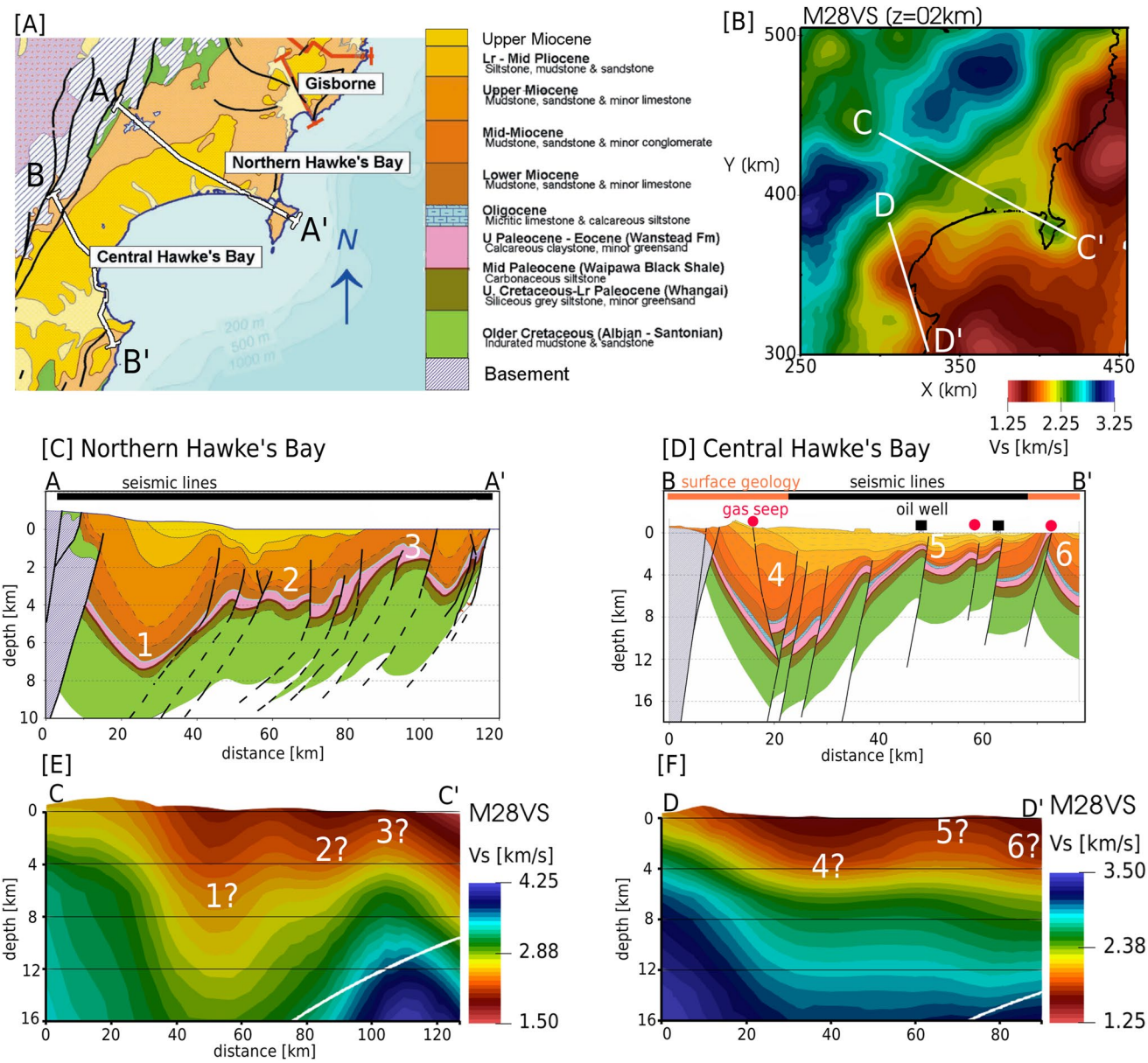

Figure 13. Geologic cross sections of Francis et al. (2004) compared with the final V_s velocity model (M28). (a) Map view of the Hawke's Bay region. Colors correspond to sedimentary rock types in the legend. A–A' and B–B' show surface traces of cross sections shown in (c) and (d). (b) 2 km depth slice of M28 V_s model. C–C' and D–D' corresponds to surface traces of cross sections shown in (e) and (f). (c) A–A' geologic cross section through Northern Hawke's Bay at 5x vertical exaggeration. Features 1, 2, and 3 used for comparisons with the velocity model in (e). Black lines represent faults, with dashed lines referring to inferred fault continuations. This cross section is interpreted from active source seismic data. (d) B–B' Central Hawke's Bay geologic cross section at 2X vertical exaggeration, derived from surface geology and seismic lines. Gas seeps and oil well locations are shown as red circles and black squares. Features 4, 5, and 6 correspond to features in (f). (e) C–C' cross section through M28 V_s model at 4x vertical exaggeration. White solid line shows the plate interface model of Williams et al. (2013). Corresponding velocity features 1, 2, and 3 are from (c). (f) D–D' cross section through M28 V_s model at 3x vertical exaggeration. Corresponding velocity features 4, 5, and 6 are from (d).

7.2. Along-Strike Crustal Heterogeneity

Material heterogeneity along the strike of the Hikurangi has been proposed as an explanation for the observed locked-to-creeping transition zone of the plate interface (Reyners et al., 2017). In the NZ-Wide2.2 velocity model, Reyners et al. (2017) relate high V_p/V_s (> 1.73) in the north with low slip rate deficit (blue interface line in Figure 14a). They interpret the southward transition to low V_p/V_s values (< 1.73) as a progressive decrease in upper plate water content (red interface line in Figure 14a). In conjunction with relocated seismicity, Reyners

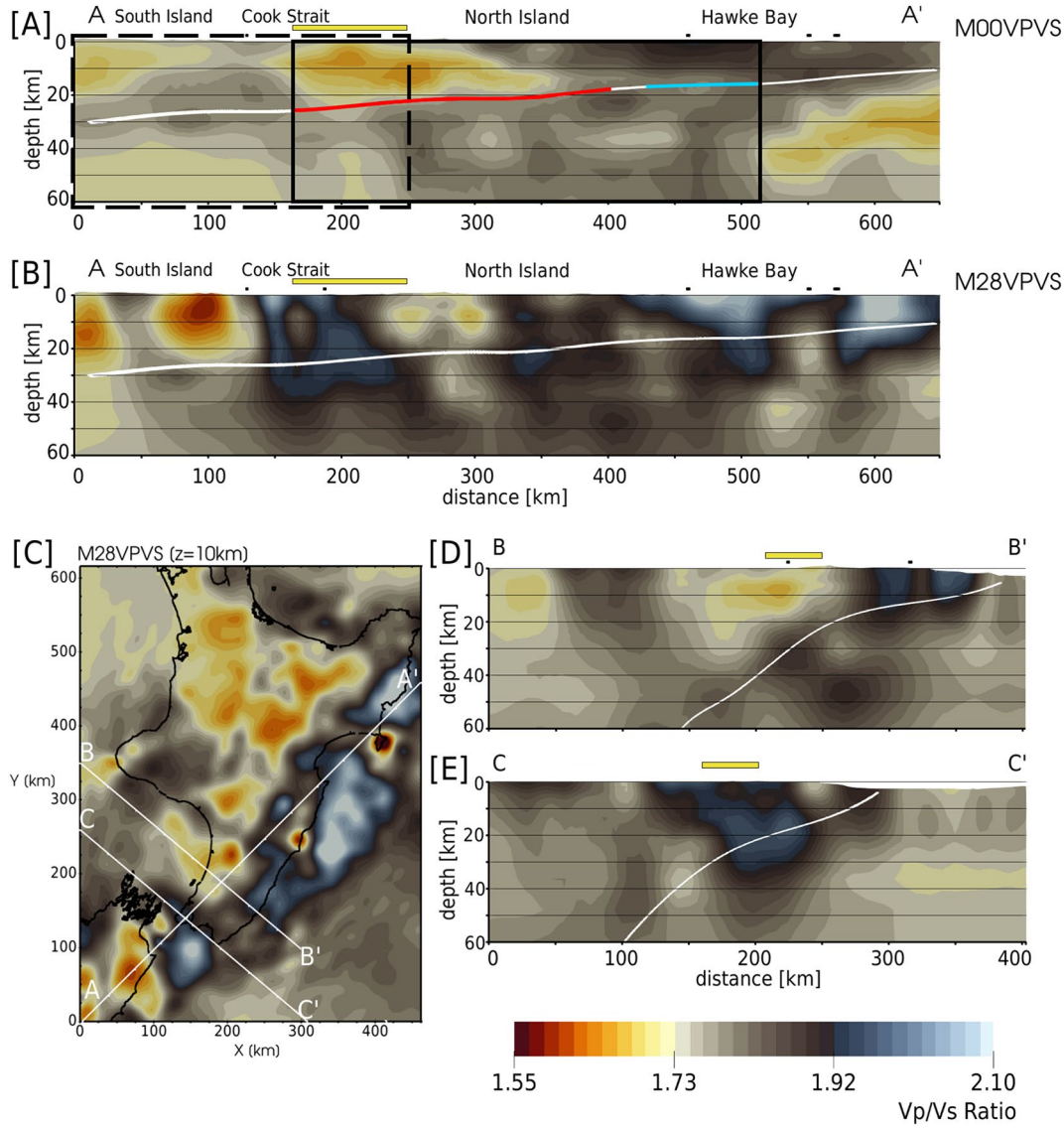

Figure 14. Along-strike heterogeneity of V_p/V_s represented by three vertical cross sections (A–A', B–B', C–C') whose lines are shown in (c). Cross sections are shown to 60 km depth with 2x vertical exaggeration; solid white line corresponds to the plate interface model of Williams et al. (2013); solid yellow line shows the approximate location of Rakaia terrane (Figure 12a). (a) M00 V_p/V_s A–A' cross section. Black outlines correspond to approximate bounds of Figure 5 (solid) and Figure 6 (dashed) of Reyners et al. (2017). Approximate geographic locations are annotated above the plot. Red interface line marks where slip rate deficit is >20 mm/yr. Blue line marks where slip rate deficit is <10 mm/yr (Wallace, Barnes, et al., 2012; Reyners et al., 2017). (b) M28 V_p/V_s A–A' cross section. (c) M28 V_p/V_s at 10 km depth. (d) M28 V_p/V_s B–B' cross section. (e) M28 V_p/V_s C–C' cross section.

et al. (2017) proposed that along-strike fluid distributions arise from variations in permeability of the overlying basement terranes, postulating that the Rakaia terrane (solid yellow lines in Figure 14a, 14b, 14d and 14e) acts as a permeability barrier, surrounded by a more permeable Pahau terrane that allows water to migrate from subducted rocks into the upper lower plate (Figure 12a).

In contrast to the findings of Reyners et al. (2017), our final V_p/V_s model does not show the same southward linear transition from high to low V_p/V_s along strike, but rather strong heterogeneity and alternating patches of high and low V_p/V_s along strike (Figure 14b). If terrane boundaries are the cause of fluid distribution in the upper plate, then we would expect to see these patches correlate to terrane transitions. The yellow line on Figure 14b denotes the approximate location of the Rakaia terrane, surrounded by the Pahau terrane (Figure 12a), showing little

correlation of V_p/V_s and terrane boundaries. Similarly strike-parallel cross sections through the Rakaia terrane show varying values of V_p/V_s (Figures 14d and 14e).

The final velocity model suggests that V_p/V_s structures are correlated more to the juxtaposition of a fractured, low-velocity (high-V_p/V_s), water-saturated forearc, against more competent, high-velocity (low-V_p/V_s), basement terranes of the North and the South Islands (Figure 14b). Although we do observe that terrane boundaries exert control on upper plate heterogeneity through velocity structures (Section 7.1), permeability control by upper plate composition seems to be insufficient to explain the heterogeneous, long-wavelength V_p/V_s structures we observe.

7.3. Cook Strait Velocity Gradients

A strong velocity gradient in Cook Strait is imaged in the upper 10–15 km. It is defined by a low-velocity anomaly in Cook Strait, with steep, near-linear gradients near the coasts of the North and South Islands (labels N and S in Figure 15). On the basis of negative gravity anomalies and significant two way travel times (3–4 s TWT), Uruski (1992) identified three sedimentary basins in Cook Strait, suggesting >3 km deep sediment fills. Low-velocity sediments within these deep basin structures may be the source of the shallow, low velocities imaged in Cook Strait. In cross section, the gradients between these inferred basins and the North and South Islands are significant (Figures 15e and 15f). The northern boundary shows gradual relief with velocities reducing from approximately 3 km/s to 2 km/s across the transition (Figure 15c). The southern boundary separating Cook Strait and South Island shows a stronger contrast from 4 km/s to 2 km/s over 50 km distance (Figure 15e).

We use a PSF to probe resolution in this region (Figures 15c and 15g). The perturbation $\delta\mathbf{m}$ is a shallow (3 km depth), negative velocity perturbation, whose full-width is chosen to match the size of the low-velocity anomaly (Figure 15a). The amplitude of the resulting PSF is peaked offset from the perturbation and smeared in a roughly northeast–southwest direction (Figure 15b). In cross section the PSF suggests that a shallow velocity perturbation will be smeared a few km to depth. We interpret the results of the point spread function to suggest that the broad structure (50 km) of the low-velocity anomaly in Cook Strait is well-resolved, however the exact location and spatial extent of these features will be affected by smearing and lateral uncertainty.

These velocity gradients can be corroborated with additional evidence. Henrys et al. (2020) observe an abrupt crustal transition zone (hatched pattern in Figure 15a; black rectangles in Figures 15c and 15e), which coincides with our northern velocity gradient. This transition zone has previously been proposed as the ancient, rotated, Alpine-Wairau fault (Barnes & Audru, 1999; Little & Roberts, 1997). A structural boundary here has also been proposed to be the faulted edge of North Island basement rocks (Holdgate & Grapes, 2015). Seismicity in the South Island appears to correlate with the southern velocity gradient (Figure 15a). The northern extent of large magnitude (M > 5) earthquakes (GeoNet) and relocated Kaikōura aftershock seismicity (Figure 15b; Chamberlain et al., 2021) seem to coincide with the structural contrast here. This may be related to the sharp transition from exposed continental crust in the South Island to deep sedimentary basins in Cook Strait.

7.4. Taupō Volcanic Zone Velocity Anomalies

The central TVZ, located between between the Taupō and Okataina calderas, is an exceptionally productive region of silicic volcanism, while andesitic volcanism is dominant to the north and south (Figure 16a; Wilson et al., 2009). The final velocity model features a low-velocity zone (V_s < 3 km/s) extending from Ruapehu to White Island in a northeast–southwest trend, bounded by high velocities on either side (V_s > 3.25 km/s; Figure 16a). Broad-scale velocity features in the TVZ correlate well with spatial boundaries related to geophysical and volcanic domains defined in previous studies.

The Young TVZ is denoted by the solid black lines in Figure 16a and defines a region where intense volcanic and geothermal activity has occurred in the last 350 kyr (Wilson et al., 1995). The Young TVZ best outlines the lowest velocities (V_s < 2.75 km/s) seen in this region. Negative gravity anomalies in the TVZ have been inferred to correlate with collapse areas and large caldera complexes (purple outlines in Figure 16a; Stagpoole et al., 2020), and the individual low-velocity lobes seen within the Young TVZ may represent the juxtaposition of caldera infills and exposed basement rocks. Geothermal fluids within the crust may also explain these low-velocity features which is supported by active geothermal production in the central TVZ (Chambefort et al., 2014). The old TVZ

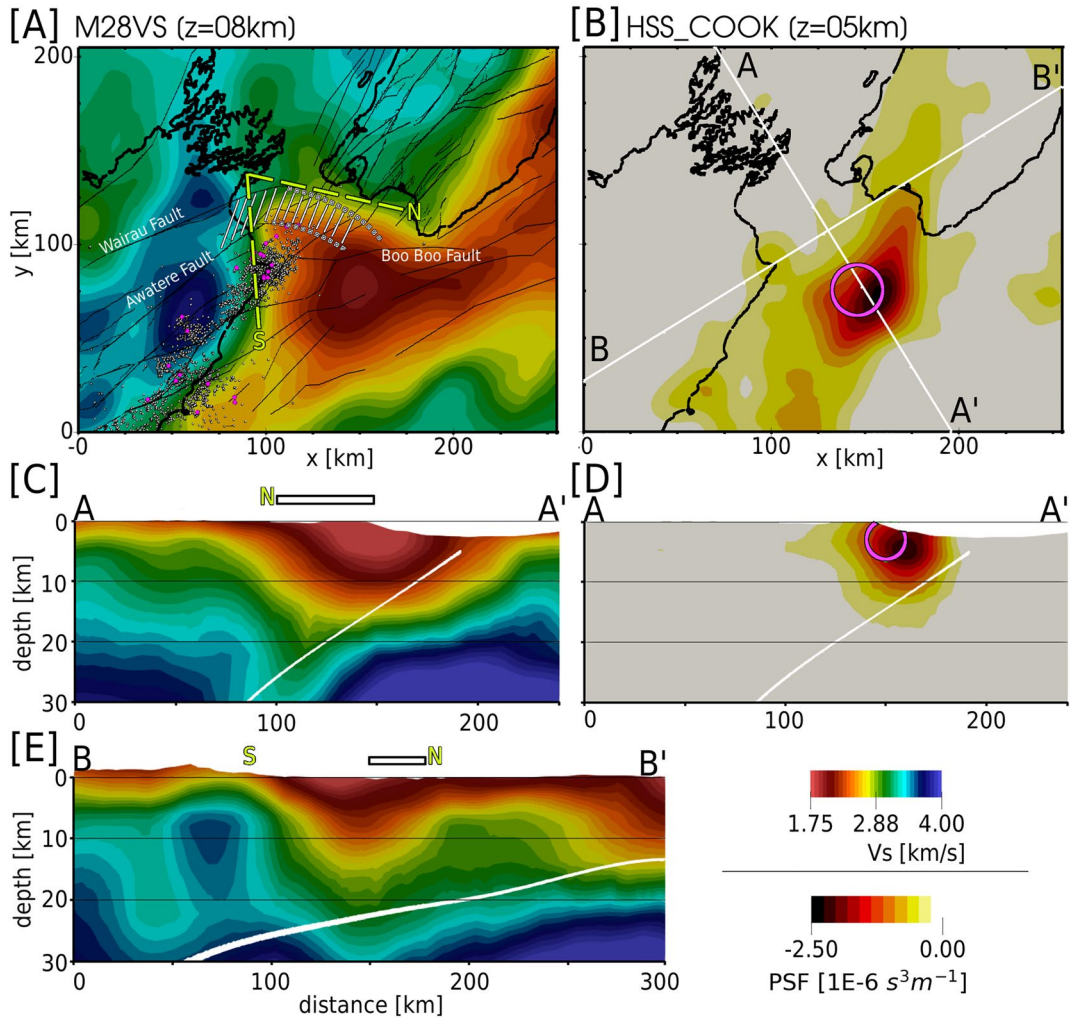

Figure 15. Cook Strait velocity gradient and point spread test. (a) M28 V_s at 8 km depth. Northern (N) and southern (S) velocity gradients are marked by green dashed lines. Relocated Kaikōura aftershocks with depth >20 km and $M > 3$ are shown as white circles (Chamberlain et al., 2021). Earthquakes M>5.5 are colored pink (GeoNet). The crustal transition zone (CTZ) identified by Henrys et al. (2020) is marked by the hatched pattern. (b) PSF at 5 km depth. Horizontal full width of input Gaussian perturbation is shown as an open pink circle. Surface traces A–A' and B–B' correspond to cross sections in C–E. (c) M28 V_s A–A' cross section. Locations of northern velocity gradient (N) and CTZ are marked. (d) H_{SS} A–A' cross section. Vertical full width of input Gaussian perturbation is shown as the open pink circle. (e) M28 V_s B–B' cross section. Locations of northern velocity gradient (N), southern velocity gradient (S), and CTZ are marked. All cross sections shown with 3x vertical exaggeration. White solid lines denote the plate interface model of Williams et al. (2013).

(dashed black line in Figure 16a; Wilson et al., 1995) defines the region of active volcanism in the last 2 Myr and captures the general low-velocity zone that extends beyond the Young TVZ ($V_s < 3.25$ km/s), while the triangular shaped region of previously noted positive gravity anomalies (white dashed line in Figure 16a; Stern, 1985), known as the Central Volcanic Region (CVR), corresponds well with the high-velocity V-shape bounding the low velocities here.

We perform a point spread test for one of the shallow, low-velocity lobes within the TVZ (Figures 16c and 16d). The recovered PSF shows extensive lateral smearing along-rift, offering both caution and guidance in interpreting features here. One peak of the PSF is located near the input perturbation, however high PSF amplitudes can also be seen below White Island, and along the western edge of the TVZ (Figure 16c). This suggests that strong heterogeneities within the TVZ may consequently map to structure offshore and outside of the volcanic region. This is reinforced in cross-section (Figure 16d), where the lateral uncertainty is evident in the separation of the input

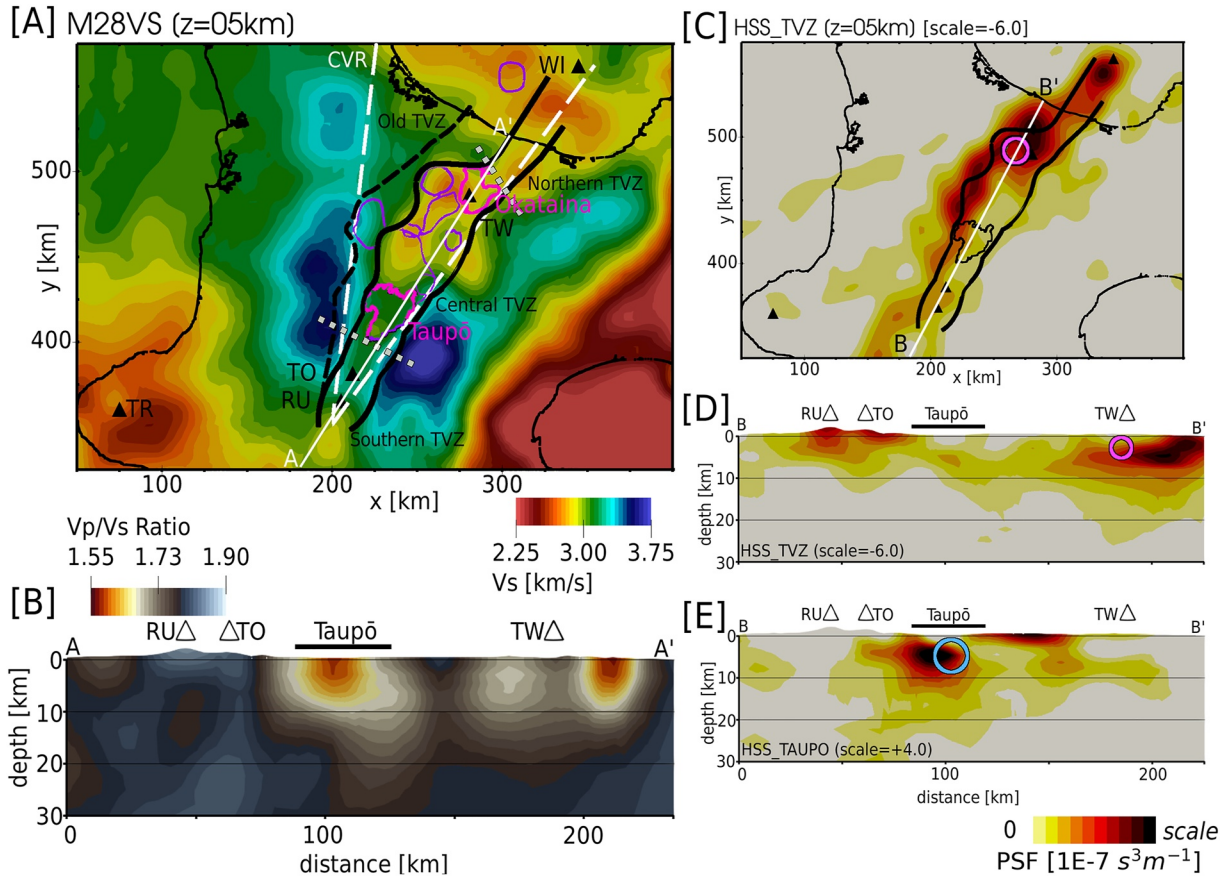

Figure 16. Taupō Volcanic Zone (TVZ) velocity anomalies and point spread test. (a) M28 V_s at 5 km depth. Solid black lines mark the extent of the Young TVZ, separated into southern, central, and northern segments (gray dotted lines). Dashed black line shows the western boundary of the Old TVZ, which shares its eastern boundary with the Young TVZ. The white dashed lines show the Central Volcanic Region (CVR). Black triangles mark locations of volcanoes discussed in text (TR, Taranaki; RU, Ruapehu; TO, Tongariro; TW, Tarawera; WI, White Island). Purple lines show locations of low gravity anomalies that correlate with topographic extents of geologically inferred calderas (Stagpoole et al., 2020). (b) M28 V_p/V_s A–A' cross section. (c) Point spread function (PSF) at 5 km depth for a negative velocity perturbation placed within the TVZ. The horizontal full width of the input perturbation is denoted by the open pink circle. (d) PSF B–B' cross section, same as in (c). (e) PSF B–B' cross section for a positive-velocity perturbation at 5 km depth below lake Taupō (blue circle).

perturbation and the recovered PSF. The perturbation is resolved almost 20 km northeast of its actual location, suggesting that resolution of features in the TVZ may have high spatial uncertainty.

At depth, previous geophysical studies have imaged a high-conductivity, plume-like structure beneath the rift axis between Taupō and Okataina (Heise et al., 2010), and low Q_s values underlying caldera structures in the central rift structure (Eberhart-Phillips, Bannister, & Reyners, 2020). We use V_p/V_s to explore the TVZ at depth due to its sensitivity to fluids (Figure 16b). In volcanic regions, high V_p/V_s ratios can be linked to the presence of geothermal fluids or partial melt in the crust (e.g., Husen et al., 2004), while low V_p/V_s have been linked to the presence of a substantial amount of free quartz in basement rock (Christensen, 1996; Ukawa & Fukao, 1981) or gaseous pore fluids in the crust (e.g., Husen et al., 2004).

A rift-parallel V_p/V_s cross section shows heterogeneous V_p/V_s structures in the TVZ that appear to spatially correlate with the varying types of volcanism here (Figure 16b). To the south, columns of high V_p/V_s (> 1.8) are imaged rising up to the andesitic Ruapehu and Tongariro volcanos. These may represent a blurred, long-wavelength image of distributed melt pockets linked to these overlying volcanoes (Figure 16b). In contrast, we image shallow (> 8 km), low V_p/V_s (< 1.6) features below the gas-rich silicic Taupō caldera and northeast of Okataina caldera (Figure 16b). Previous studies suggest that large melt chambers exist below these active rhyolitic calderas (e.g., S. Barker et al., 2020; Illsley-Kemp et al., 2021), however we would expect regions of partial melt to exhibit high, not low, V_p/V_s signatures. The presence of gas at depth has been used explain such

low-V_p/V_s values (e.g., Husen et al., 2004) and may offer one potential explanation in which gas released by rhyolitic melt at depth fills the pore space above the inferred melt chambers, leading to the low-V_p/V_s anomalies we image.

A PSF for the Taupō caldera shows that recovery of a positive velocity perturbation below lake Taupō results in slightly offset but relatively constrained recovery, suggesting this low-V_p/V_s feature is moderately resolved. In contrast, the PSF nearby Okataina caldera (Figure 16d) suggests that an anomaly below the caldera will not be resolved in the correct location, providing a possible explanation for the high-V_p/V_s signature located northeast of, rather than directly below, Okataina caldera.

7.5. Implications of Strong Velocity Changes

The large (±30%) recovered velocity changes with respect to the initial NZ-Wide2.2 velocity model have the potential to impact studies that rely on 3D velocity structures as input, such as inversions of shallow subduction slow slip events, earthquake relocations, ground motion prediction simulations, and estimations of seismic hazard.

Using the NZ-Wide velocity model, Williams and Wallace (2018) generated Green's functions and estimated the magnitude of slow slip events on the Hikurangi subduction interface. They found that introducing heterogeneous elastic properties had significant effects with respect to an interface model with homogeneous material properties, increasing seismic potency by 58% or more. Our revised V_s model has heterogeneous changes in elastic properties that would affect slip estimations. Increased offshore resolution of the shallow subduction interface should also increase heterogeneity of interface properties, leading to greater spatial variations in estimations of expected slip.

Earthquake relocation is an important method for constraining relative or absolute locations of seismic events. Relocated earthquake catalogs of small magnitude events ($M \leq 4$) can be used to map fault structures (e.g., Lanza et al., 2019), infer pore fluid pressures, or spatially constrain large-scale tectonic features (e.g., Reyners et al., 2017). Methods like nonlinear location inversion (Lomax et al., 2000) rely on input 3D velocity models to search for optimum earthquake locations; consequently the NZ-Wide velocity model has been employed in New Zealand earthquake relocation studies (e.g., Bannister et al., 2011; Lanza et al., 2019; Reyners et al., 2011). Velocity changes introduced in our study may affect inferred earthquake locations, for example, for near-offshore or very shallow earthquakes.

Ground motion simulations can be used to constrain expected ground shaking for large potential earthquakes (e.g., Bradley et al., 2017; Graves et al., 2011). In these simulations, the underlying velocity model controls 3D wave propagation effects, such as amplified shaking in sedimentary basins or directivity caused by topography or subsurface structure. In the South Island, New Zealand, for example, ground motion simulations of a large Alpine fault rupture show significant rupture directivity and basin-generated surface waves that result in notable increases in peak ground velocities (Bradley et al., 2017). Similarly, velocity models in southern California have been used to constrain strong ground motion of potential fault ruptures to estimate seismic hazard (Graves et al., 2011).

Our updated velocity model, resultant wave propagation simulations, and predictions of faults and ground shaking, have the potential to impact the estimation of seismic hazards in New Zealand. For example, observed long-duration ground shaking in offshore regions should be more accurately captured by the updated velocity structures (Kaneko et al., 2019). Similarly, Ellis et al. (2017) show that velocity gradients at depth can be used to identify previously unmapped faults which may host large, damaging earthquakes. Improved crustal resolution in our velocity model would assist in such studies which make use of 3D velocity structures. Future characterization of high-frequency (>1 Hz) ground motion, however, would require refinement of short-scale structures, something only possible with much denser deployments of seismic stations.

8. Conclusions

We perform 28 L-BFGS iterations to improve a starting 3D velocity model of the North Island of New Zealand using spectral element and adjoint methods. Waveforms for 60 events recorded on up to 88 broadband seismic stations are compared with synthetic waveforms within automatically selected time windows and quantified using

a traveltime cross-correlation objective function. Measurements are made on up to 1,800 source-receiver pairs, for a final waveform period range of 4–30 s. Computational cost totaled ~500,000 CPU-hours over the course of the inversion.

The final velocity model (M28) is defined by updated V_p and V_s. Net model updates show large—up to ±30%—heterogeneous velocity changes with respect to the initial V_s model. In general, velocities are slowed down, existing features are sharpened, and new velocity anomalies are imaged. Resolution analyses using point spread function and a zeroth moment test show that model updates are resolved best in terms of V_s, on land and in the near-offshore region, and above ~30 km depth. Comparisons with geologic cross sections (Figure 13) show that the final model is able to resolve shallow velocity structure (>5 km depth). Point spread functions used to test robustness of individual features in the final velocity model show varying degrees of resolution.

Based on the strong velocity changes shown in Figures 5 and 6, we observe that the application of adjoint tomography has resulted in improved resolution of shallow (< 15 km) crustal structure and small-scale (<50 km) velocity anomalies within our domain (Figure 4). We attribute a significant portion of this increased sensitivity to the predominant use of surface wave measurements in the inversion, which fortuitously provide increased sensitivity to shallow structure and the offshore forearc region using only land-based measurements. These additional sections of the waveform, coupled with finite-frequency effects built in to adjoint tomography, have provided increased sensitivity to regions and anomalies that were not accessible with the more classical tomographic approach used to derive the initial model.

We interpret the most striking velocity changes in the context of known geology and tectonics. Shallow V_s velocity structures correlate well with New Zealand basement terranes, and sedimentary and volcanic cover. Large-scale, along-strike V_p/V_s structures within a well-resolved region of our updated model show increased heterogeneity that contrasts with previous interpretations in which heterogeneous terrane permeability controls interface locking. In Cook Strait we image steep-sided, deep sedimentary basins as strong velocity contrasts between Cook Strait and the North and South Islands. In the Taupō Volcanic Zone we image slow, shallow velocities at the surface that generally correlate with low-gravity anomalies inferred as caldera locations, as well as heterogeneous V_p/V_s structures at depth that show good correlation with observed volcanic compositions.

The velocity models presented in this study provide further constraint on enigmatic tectonic properties of the Hikurangi Subduction Zone. New Zealand source–receiver coverage ultimately limits the resolving power of our methods, and future work may target improved resolution through denser, more uniform receiver coverage. Additionally, more focused efforts to fit short-period (~2 s) waveforms, for example, through careful curation of input data, may improve resolution of small-scale (< 5 km) features. New Zealand velocity models, as derived in this study, are important for understanding Earth structure and have first-order impact on other work including earthquake relocations, megathrust slip research, and estimations of seismic hazard.

Appendix A

Although the windowing algorithm employed in our automated workflow does not require explicit labelling of seismic phases, it is useful to investigate which phases are included in our data set. To do so, we explore apparent travel times and velocities. Phase arrivals are approximated by the relative start time of measurement windows and corresponding source–receiver distance (Figures A1a and A1c). Apparent velocities (Figures A1b and A1d) are calculated as the ratio of source–receiver distance and relative start time. Although apparent velocities show distinct peaks at direct arrival and surface wave velocities (Figure A1d), the scatter among points on the travel time plot (Figure A1c) indicate that more complex phases are likely included in our data set.

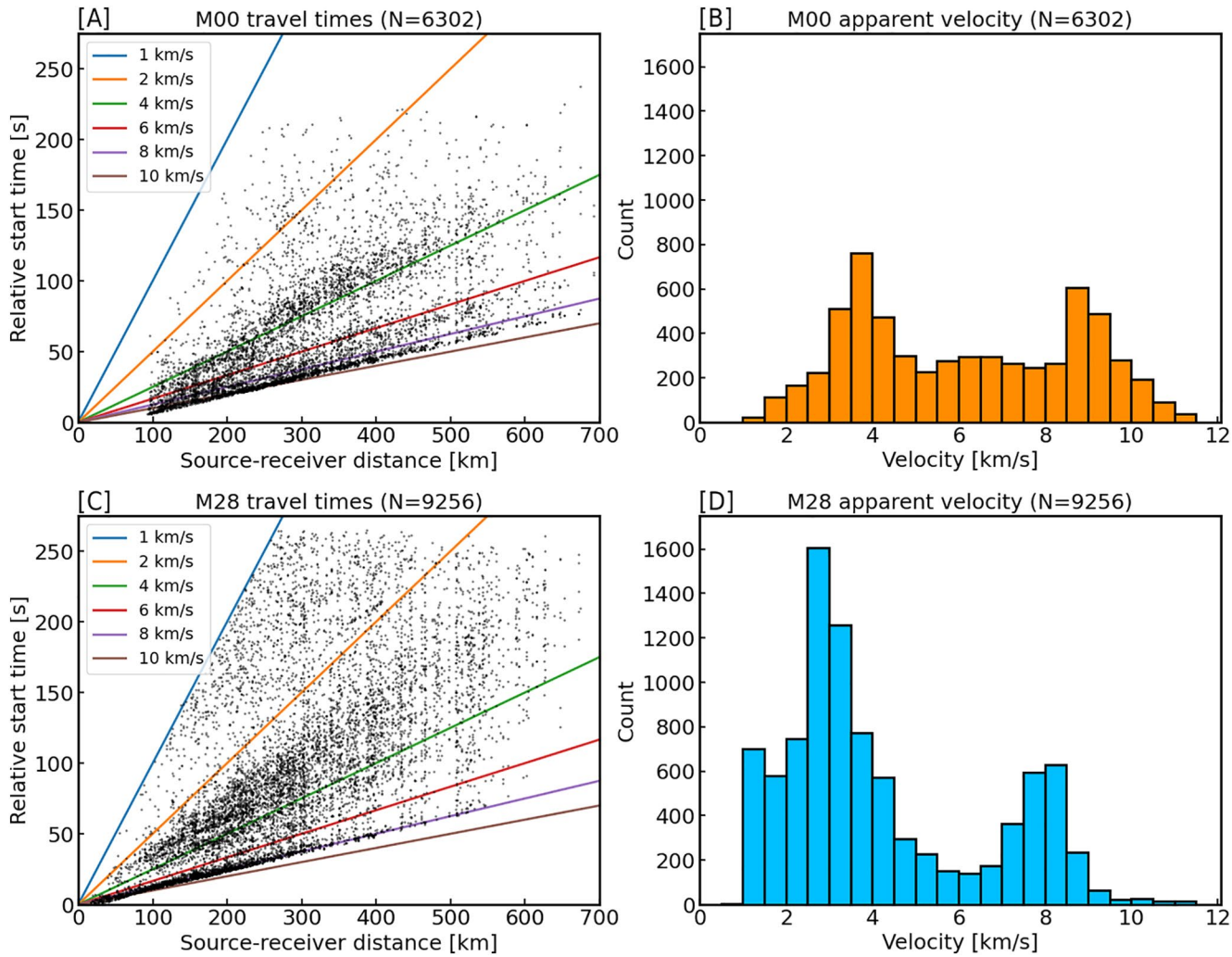

Figure A1. Travel times and apparent velocities comparing the initial (M00) and final (M28) models. (a) Initial model travel times for misfit windows chosen for 15–30 s waveforms. Colored lines show lines of constant velocity. (b) Apparent velocity histogram, calculated from (a). (c) Final model apparent travel times for 4–30 s waveforms. (d) Final model apparent velocities, calculated from (c).

Data Availability Statement

Temporary network seismic waveform data sets used in this research are available in these intext data citation references: Bannister (2009), Bannister and Bourguignon (2011), Henrys et al. (2013), Kaneko and Chow (2017). The starting (M00) and final (M28) velocity models, alongside associated metadata, are publicly available through the IRIS Earth Model Collaboration (EMC) repository (https://doi.org/10.17611/dp/emc.2021.nzatomn-northvpvs.1). BEACON deployment continuous waveform data and metadata will be made available through IRIS (Kaneko & Chow, 2017). Waveform data from the New Zealand permanent network (GeoNet) and the SAHKE deployment were accessed publicly via IRIS FDSN webservices.

Acknowledgments
This work was funded by a Rutherford Discovery Fellowship (GNS1601) and Marsden Fund (GNS1501) awarded by the Royal Society of New Zealand Te Apārangi. We thank Donna Eberhart-Phillips for providing the latest NZ-Wide2.2 3D velocity model. We acknowledge John Ristau for providing earthquake moment

References

Akcelik, V., Bielak, J., Biros, G., Epanomeritakis, I., Fernandez, A., Ghattas, O., et al. (2003). High resolution forward and inverse earthquake modeling on terascale computers. In *Proceedings of the 2003 ACM/IEEE conference on supercomputing* (pp. 52). https://doi.org/10.1145/1048935.1050202

Audet, P., Bostock, M. G., Christensen, N. I., & Peacock, S. M. (2009). Seismic evidence for overpressured subducted oceanic crust and megathrust fault sealing. *Nature*, *457*(7225), 76–78. https://doi.org/10.1038/nature07650

Bannister, S. (2009). *Deep geothermal HADES seismic array*. International Federation of Digital Seismograph Networks. https://doi.org/10.7914/SN/Z8_2009

tensors. BEACON field deployment and servicing was performed by: Yoshihiro Kaneko, Bryant Chow, Jonathan Hanson, Dan Whitaker, Rory Hart, Conrad Burton, Garth Archibald, Dan Bassett, Kris O'Brien, Tim McDougall, Hubert Zal, Danielle Lindsay, and Jesse Kearse. We thank individual land owners and forestry companies for allowing us onto their land. All simulation work was performed on the New Zealand eScience Infrastructure's HPC, Māui. We thank Alexander Pletzer for helping us optimize SPECFEM3D Cartesian on Māui. We thank Finnigan Illsley-Kemp, Calum Chamberlain, Laura Wallace, Susan Ellis, Tim Little and Carolyn Boulton for fruitful discussions during interpretations of the final velocity model. We thank the Associate Editor and two anonymous reviewers for helping improve the original manuscript through constructive feedback.

Bannister, S., & Bourguignon, S. (2011). *Gisborne-Mahia seismic tremor array*. International Federation of Digital Seismograph Networks. https://doi.org/10.7914/SN/ZX_2011

Bannister, S., Fry, B., Reyners, M., Ristau, J., & Zhang, H. (2011). Fine-scale relocation of aftershocks of the 22 February Mw 6.2 Christchurch earthquake using double-difference tomography. *Seismological Research Letters*, *82*(6), 839–845. https://doi.org/10.1785/gssrl.82.6.839

Barker, D., Sutherland, R., Henrys, S., & Bannister, S. (2009). Geometry of the Hikurangi subduction thrust and upper plate, North Island, New Zealand. *Geochemistry, Geophysics, Geosystems*, *10*(2). https://doi.org/10.1029/2008gc002153

Barker, S., Rowe, M. C., Wilson, C. J., Gamble, J. A., Rooyakkers, S. M., Wysoczanski, R. J., et al. (2020). What lies beneath? Reconstructing the primitive magmas fueling voluminous silicic volcanism using olivine-hosted melt inclusions. *Geology*, *48*(5), 504–508. https://doi.org/10.1130/g47422.1

Barnes, P. M., & Audru, J.-C. (1999). Quaternary faulting in the offshore Flaxbourne and Wairarapa basins, Southern Cook Strait, New Zealand. *New Zealand Journal of Geology and Geophysics*, *42*(3), 349–367. https://doi.org/10.1080/00288306.1999.9514851

Barnes, P. M., Lamarche, G., Bialas, J., Henrys, S., Pecher, I., Netzeband, G. L., et al. (2010). Tectonic and geological framework for gas hydrates and cold seeps on the Hikurangi subduction margin, New Zealand. *Marine Geology*, *272*(1–4), 26–48. https://doi.org/10.1016/j.margeo.2009.03.012

Becker, J., Sandwell, D., Smith, W., Braud, J., Binder, B., Depner, J., et al. (2009). Global bathymetry and elevation data at 30 arc seconds resolution: SRTM30_PLUS. *Marine Geodesy*, *32*(4), 355–371. https://doi.org/10.1080/01490410903297766

Bell, R., Holden, C., Power, W., Wang, X., & Downes, G. (2014). Hikurangi margin tsunami earthquake generated by slow seismic rupture over a subducted seamount. *Earth and Planetary Science Letters*, *397*, 1–9. https://doi.org/10.1016/j.epsl.2014.04.005

Bozdağ, E., Peter, D., Lefebvre, M., Komatitsch, D., Tromp, J., Hill, J., et al. (2016). Global adjoint tomography: First-generation model. *Geophysical Journal International*, *207*(3), 1739–1766.

Bozdağ, E., Trampert, J., & Tromp, J. (2011). Misfit functions for full waveform inversion based on instantaneous phase and envelope measurements. *Geophysical Journal International*, *185*(2), 845–870.

Bradley, B. A., Bae, S. E., Polak, V., Lee, R. L., Thomson, E. M., & Tarbali, K. (2017). Ground motion simulations of great earthquakes on the Alpine fault: Effect of hypocentre location and comparison with empirical modelling. *New Zealand Journal of Geology and Geophysics*, *60*(3), 188–198. https://doi.org/10.1080/00288306.2017.1297313

Bunks, C., Saleck, F. M., Zaleski, S., & Chavent, G. (1995). Multiscale seismic waveform inversion. *Geophysics*, *60*(5), 1457–1473. https://doi.org/10.1190/1.1443880

Carter, R. M., & Naish, T. R. (1998). A review of Wanganui basin, New Zealand: Global reference section for shallow marine, Plio–Pleistocene (2.5–0 Ma) cyclostratigraphy. *Sedimentary Geology*, *122*(1–4), 37–52. https://doi.org/10.1016/s0037-0738(98)00097-9

Chambefort, I., Lewis, B., Wilson, C., Rae, A., Coutts, C., Bignall, G., et al. (2014). Stratigraphy and structure of the Ngatamariki geothermal system from new zircon U–Pb geochronology: Implications for Taupō Volcanic Zone evolution. *Journal of Volcanology and Geothermal Research*, *274*, 51–70. https://doi.org/10.1016/j.jvolgeores.2014.01.015

Chamberlain, C. J., Frank, W., Lanza, F., Townend, J., & Warren-Smith, E. (2021). Illuminating the pre-, co-, and post-seismic phases of the 2016 M7.8 Kaikoūra earthquake with 10 years of seismicity. *Journal of Geophysical Research: Solid Earth*, e2021JB022304. https://doi.org/10.1029/2021JB022304

Chen, M., Niu, F., Liu, Q., Tromp, J., & Zheng, X. (2015). Multiparameter adjoint tomography of the crust and upper mantle beneath East Asia: 1. Model construction and comparisons. *Journal of Geophysical Research: Solid Earth*, *120*(3), 1762–1786. https://doi.org/10.1002/2014jb011638

Chow, B., Kaneko, Y., Tape, C., Modrak, R., & Townend, J. (2020). An automated workflow for adjoint tomography — waveform misfits and synthetic inversions for the North Island, New Zealand. *Geophysical Journal International*, *223*(3), 1461–1480. https://doi.org/10.1093/gji/ggaa381

Chow, B., Kaneko, Y., & Townend, J. (2022). Evidence for deeply-subducted lower-plate seamounts at the Hikurangi subduction margin: Implications for seismic and aseismic behavior. *Journal of Geophysical Research: Solid Earth*. (companion manuscript). https://doi.org/10.1029/2021JB022866

Christensen, N. I. (1996). Poisson's ratio and crustal seismology. *Journal of Geophysical Research*, *101*(B2), 3139–3156. https://doi.org/10.1029/95jb03446

Cochran, U., Berryman, K., Zachariasen, J., Mildenhall, D., Hayward, B., Southall, K., et al. (2006). Paleoecological insights into subduction zone earthquake occurrence, Eastern North Island, New Zealand. *GSA Bulletin*, *118*(9–10), 1051–1074. https://doi.org/10.1130/b25761.1

Collot, J.-Y., Delteil, J., Lewis, K. B., Davy, B., Lamarche, G., Audru, J.-C., et al. (1996). From oblique subduction to intra-continental transpression: Structures of the Southern Kermadec-Hikurangi margin from multibeam bathymetry, side-scan sonar and seismic reflection. *Marine Geophysical Researches*, *18*(2), 357–381. https://doi.org/10.1007/bf00286085

Dahlen, F., & Baig, A. M. (2002). Fréchet kernels for body-wave amplitudes. *Geophysical Journal International*, *150*(2), 440–466. https://doi.org/10.1046/j.1365-246x.2002.01718.x

Dahlen, F., Hung, S.-H., & Nolet, G. (2000). Fréchet kernels for finite-frequency traveltimes—I. Theory. *Geophysical Journal International*, *141*(1), 157–174. https://doi.org/10.1046/j.1365-246x.2000.00070.x

Darby, D. J., Hodgkinson, K. M., & Blick, G. H. (2000). Geodetic measurement of deformation in the Taupo Volcanic Zone, New Zealand: The North Taupo network revisited. *New Zealand Journal of Geology and Geophysics*, *43*(2), 157–170. https://doi.org/10.1080/00288306.2000.9514878

Davy, B., Hoernle, K., & Werner, R. (2008). Hikurangi Plateau: Crustal structure, rifted formation, and Gondwana subduction history. *Geochemistry, Geophysics, Geosystems*, *9*(7). https://doi.org/10.1029/2007gc001855

DeMets, C., Gordon, R. G., Argus, D. F., & Stein, S. (1994). Effect of recent revisions to the geomagnetic reversal time scale on estimates of current plate motions. *Geophysical Research Letters*, *21*(20), 2191–2194. https://doi.org/10.1029/94gl02118

Dreger, D. S. (2003). TDMT_INV: Time domain seismic moment tensor inversion. In *International geophysics* (Vol. 81, pp. 1627). Elsevier. https://doi.org/10.1016/s0074-6142(03)80290-5

Eberhart-Phillips, D., & Bannister, S. (2010). 3-D imaging of Marlborough, New Zealand, subducted plate and strike-slip fault systems. *Geophysical Journal International*, *182*(1), 73–96. https://doi.org/10.1111/j.1365-246x.2010.04621.x

Eberhart-Phillips, D., & Bannister, S. (2015). 3-D imaging of the Northern Hikurangi subduction zone, New Zealand: Variations in subducted sediment, slab fluids and slow slip. *Geophysical Journal International*, *201*(2), 838–855. https://doi.org/10.1093/gji/ggv057

Eberhart-Phillips, D., Bannister, S., & Reyners, M. (2017). Deciphering the 3-D distribution of fluid along the shallow Hikurangi subduction zone using P-and S-wave attenuation. *Geophysical Journal International*, *211*(2), 1032–1045. https://doi.org/10.1093/gji/ggx348

Eberhart-Phillips, D., Bannister, S., & Reyners, M. (2020). Attenuation in the mantle wedge beneath super-volcanoes of the Taupō volcanic zone, New Zealand. *Geophysical Journal International*, *220*(1), 703–723. https://doi.org/10.1093/gji/ggz455

Eberhart-Phillips, D., Bannister, S., Reyners, M., & Henrys, S. (2020). New Zealand wide model 2.2 seismic velocity and Qs and Qp models for New Zealand. [dataset]. Zenodo. https://doi.org/10.5281/zenodo.3779523
Eberhart-Phillips, D., & Fry, B. (2017). A new scheme for joint surface wave and earthquake travel-time inversion and resulting 3-D velocity model for the Western North Island, New Zealand. *Physics of the Earth and Planetary Interiors*, *269*, 98–111. https://doi.org/10.1016/j.pepi.2017.05.014
Eberhart-Phillips, D., & Fry, B. (2018). Joint local earthquake and teleseismic inversion for 3-D velocity and Q in New Zealand. *Physics of the Earth and Planetary Interiors*, *283*, 48–66. https://doi.org/10.1016/j.pepi.2018.08.005
Eberhart-Phillips, D., Han, D.-H., & Zoback, M. D. (1989). Empirical relationships among seismic velocity, effective pressure, porosity, and clay content in sandstone. *Geophysics*, *54*(1), 82–89.
Eberhart-Phillips, D., & Reyners, M. (1997). Continental subduction and three-dimensional crustal structure: The Northern South Island, New Zealand. *Journal of Geophysical Research*, *102*(B6), 11843–11861. https://doi.org/10.1029/96jb03555
Eberhart-Phillips, D., & Reyners, M. (2012). Imaging the Hikurangi plate interface region, with improved local-earthquake tomography. *Geophysical Journal International*, *190*(2), 1221–1242. https://doi.org/10.1111/j.1365-246x.2012.05553.x
Eberhart-Phillips, D., Reyners, M., & Bannister, S. (2015). A 3D QP attenuation model for all of New Zealand. *Seismological Research Letters*, *86*(6), 1655–1663. https://doi.org/10.1785/0220150124
Eberhart-Phillips, D., Reyners, M., Chadwick, M., & Chiu, J.-M. (2005). Crustal heterogeneity and subduction processes: 3-D Vp, Vp/Vs and Q in the Southern North Island, New Zealand. *Geophysical Journal International*, *162*(1), 270–288. https://doi.org/10.1111/j.1365-246x.2005.02530.x
Edbrooke, S., Heron, D., Forsyth, P., & Jongens, R. (2015). *Geological map of New Zealand 1:1 000 000. GNS science Geological map 2*.
Ellis, S., Van Dissen, R., Eberhart-Phillips, D., Reyners, M., Dolan, J., & Nicol, A. (2017). Detecting hazardous New Zealand faults at depth using seismic velocity gradients. *Earth and Planetary Science Letters*, *463*, 333–343. https://doi.org/10.1016/j.epsl.2017.01.038
Fagereng, R., & Ellis, S. (2009). On factors controlling the depth of interseismic coupling on the Hikurangi subduction interface, New Zealand. *Earth and Planetary Science Letters*, *278*(1–2), 120–130. https://doi.org/10.1016/j.epsl.2008.11.033
Fichtner, A., Bunge, H.-P., & Igel, H. (2006a). The adjoint method in seismology: I. Theory. *Physics of the Earth and Planetary Interiors*, *157*(1–2), 86–104. https://doi.org/10.1016/j.pepi.2006.03.016
Fichtner, A., Bunge, H.-P., & Igel, H. (2006b). The adjoint method in seismology—: II. Applications: Traveltimes and sensitivity functionals. *Physics of the Earth and Planetary Interiors*, *157*(1–2), 105–123. https://doi.org/10.1016/j.pepi.2006.03.018
Fichtner, A., Kennett, B. L., Igel, H., & Bunge, H.-P. (2009). Full seismic waveform tomography for upper-mantle structure in the Australasian region using adjoint methods. *Geophysical Journal International*, *179*(3), 1703–1725. https://doi.org/10.1111/j.1365-246x.2009.04368.x
Fichtner, A., Kennett, B. L., Igel, H., & Bunge, H.-P. (2010). Full waveform tomography for radially anisotropic structure: New insights into present and past states of the Australasian upper mantle. *Earth and Planetary Science Letters*, *290*(3–4), 270–280. https://doi.org/10.1016/j.epsl.2009.12.003
Fichtner, A., & Trampert, J. (2011a). Hessian kernels of seismic data functionals based upon adjoint techniques. *Geophysical Journal International*, *185*(2), 775–798. https://doi.org/10.1111/j.1365-246x.2011.04966.x
Fichtner, A., & Trampert, J. (2011b). Resolution analysis in full waveform inversion. *Geophysical Journal International*, *187*(3), 1604–1624. https://doi.org/10.1111/j.1365-246x.2011.05218.x
Francis, D., Bennett, D., & Courteney, S. (2004). Advances in understanding of onshore East Coast Basin structure, stratigraphic thickness and hydrocarbon generation. In *New Zealand petroleum conference proceedings* (pp. 1–20).
Graves, R., Jordan, T. H., Callaghan, S., Deelman, E., Field, E., Juve, G., et al. (2011). CyberShake: A physics-based seismic hazard model for Southern California. *Pure and Applied Geophysics*, *168*(3), 367–381. https://doi.org/10.1007/s00024-010-0161-6
Hamling, I. J., Hreinsdóttir, S., Clark, K., Elliott, J., Liang, C., & Fielding, E. (2017). Complex multifault rupture during the 2016 Mw 7.8 Kaikōura earthquake, New Zealand. *Science*, *356*(6334), eaam7194. https://doi.org/10.1126/science.aam7194
Heise, W., Caldwell, T. G., Bibby, H. M., & Bennie, S. L. (2010). Three-dimensional electrical resistivity image of magma beneath an active continental rift, Taupo Volcanic Zone, New Zealand. *Geophysical Research Letters*, *37*(10). https://doi.org/10.1029/2010gl043110
Henrys, S., Eberhart-Phillips, D., Bassett, D., Sutherland, R., Okaya, D., & Savage, M. (2020). Upper plate heterogeneity along the Southern Hikurangi Margin, New Zealand. *Geophysical Research Letters*, *47*(4), e2019GL085511. https://doi.org/10.1029/2019gl085511
Henrys, S., Reyners, M., Pecher, I., Bannister, S., Nishimura, Y., & Maslen, G. (2006). Kinking of the subducting slab by escalator normal faulting beneath the North Island of New Zealand. *Geology*, *34*(9), 777–780. https://doi.org/10.1130/g22594.1
Henrys, S., Wech, A., Sutherland, R., Stern, T., Savage, M., Sato, H., et al. (2013). SAHKE geophysical transect reveals crustal and subduction zone structure at the southern Hikurangi margin, New Zealand. *Geochemistry, Geophysics, Geosystems*, *14*(7), 2063–2083. https://doi.org/10.1002/ggge.20136
Holden, C., Kaneko, Y., D'Anastasio, E., Benites, R., Fry, B., & Hamling, I. (2017). The 2016 Kaikōura earthquake revealed by kinematic source inversion and seismic wavefield simulations: Slow rupture propagation on a geometrically complex crustal fault network. *Geophysical Research Letters*, *44*(22), 11–320. https://doi.org/10.1002/2017gl075301
Holdgate, G., & Grapes, R. (2015). Wairau basin and fault connections across Cook strait, New Zealand: Seismic and geological evidence. *Australian Journal of Earth Sciences*, *62*(1), 95–121. https://doi.org/10.1080/08120099.2015.986195
Hung, S.-H., Dahlen, F., & Nolet, G. (2001). Wavefront healing: A banana–doughnut perspective. *Geophysical Journal International*, *146*(2), 289–312. https://doi.org/10.1046/j.1365-246x.2001.01466.x
Husen, S., Smith, R. B., & Waite, G. P. (2004). Evidence for gas and magmatic sources beneath the Yellowstone volcanic field from seismic tomographic imaging. *Journal of Volcanology and Geothermal Research*, *131*(3–4), 397–410. https://doi.org/10.1016/s0377-0273(03)00416-5
Illsley-Kemp, F., Barker, S., Wilson, C. J., Chamberlain, C. J., Hreinsdóttir, S., Ellis, S., et al. (2021). Volcanic unrest at Taupoñacr volcano in 2019: Causes, mechanisms and implications. *Geochemistry, Geophysics, Geosystems*, *22*(6), e2021GC009803.
Ito, H., DeVilbiss, J., & Nur, A. (1979). Compressional and shear waves in saturated rock during water-steam transition. *Journal of Geophysical Research*, *84*(B9), 4731–4735. https://doi.org/10.1029/jb084ib09p04731
Jarrard, R. D. (1986). Relations among subduction parameters. *Reviews of Geophysics*, *24*(2), 217–284. https://doi.org/10.1029/rg024i002p00217
Kanamori, H. (1972). Mechanism of tsunami earthquakes. *Physics of the Earth and Planetary Interiors*, *6*(5), 346–359. https://doi.org/10.1016/0031-9201(72)90058-1
Kaneko, Y., & Chow, B. (2017). *Broadband East Coast Network (BEACON)*. International federation of digital seismograph networks. https://doi.org/10.7914/SN/2P_2017
Kaneko, Y., Ito, Y., Chow, B., Wallace, L., Tape, C., Grapenthin, R., et al. (2019). Ultra-long duration of seismic ground motion arising from a thick, low-velocity sedimentary wedge. *Journal of Geophysical Research: Solid Earth*, *124*(10), 10347–10359. https://doi.org/10.1029/2019jb017795

Kaneko, Y., Wallace, L., Hamling, I. J., & Gerstenberger, M. C. (2018). Simple physical model for the probability of a subduction-zone earthquake following slow slip events and earthquakes: Application to the Hikurangi megathrust, New Zealand. *Geophysical Research Letters*, *45*(9), 3932–3941. https://doi.org/10.1029/2018gl077641

King, P. R., & Thrasher, G. P. (1996). *Cretaceous-Cenozoic geology and petroleum systems of the Taranaki Basin, New Zealand* (Vol. 2). Institute of Geological & Nuclear Sciences.

Komatitsch, D., Ritsema, J., & Tromp, J. (2002). The spectral-element method, Beowulf computing, and global seismology. *Science*, *298*, 1737–1742. https://doi.org/10.1126/science.1076024

Komatitsch, D., & Tromp, J. (2002a). Spectral-element simulations of global seismic wave propagation—II. Three-dimensional models, oceans, rotation and self-gravitation. *Geophysical Journal International*, *150*(1), 303–318. https://doi.org/10.1046/j.1365-246x.2002.01716.x

Komatitsch, D., & Tromp, J. (2002b). Spectral-element simulations of global seismic wave propagation—I. Validation. *Geophysical Journal International*, *149*(2), 390–412. https://doi.org/10.1046/j.1365-246x.2002.01653.x

Komatitsch, D., Tsuboi, S., Tromp, J., Levander, A., & Nolet, G. (2005). The spectral-element method in seismology. *Geophysical Monograph-American Geophysical Union*, *157*, 205–227. https://doi.org/10.1029/157gm13

Krischer, L., Fichtner, A., Boehm, C., & Igel, H. (2018). Automated large-scale full seismic waveform inversion for North America and the North Atlantic. *Journal of Geophysical Research: Solid Earth*, *123*(7), 5902–5928. https://doi.org/10.1029/2017jb015289

Krischer, L., Fichtner, A., Zukauskaite, S., & Igel, H. (2015). Large-scale seismic inversion framework. *Seismological Research Letters*, *86*(4), 1198–1207. https://doi.org/10.1785/0220140248

Lanza, F., Chamberlain, C., Jacobs, K., Warren-Smith, E., Godfrey, H., Kortink, M., et al. (2019). Crustal fault connectivity of the Mw 7.8 2016 Kaikōura earthquake constrained by aftershock relocations. *Geophysical Research Letters*, *46*(12), 6487–6496. https://doi.org/10.1029/2019gl082780

Lewis, K., & Pettinga, J. (1993). The emerging, imbricate frontal wedge of the Hikurangi margin. *Sedimentary Basins of the World*, *2*, 225–250.

Litchfield, N., Ellis, S., Berryman, K., & Nicol, A. (2007). Insights into subduction-related uplift along the Hikurangi Margin, New Zealand, using numerical modeling. *Journal of Geophysical Research*, *112*(F2). https://doi.org/10.1029/2006jf000535

Litchfield, N., Van Dissen, R., Sutherland, R., Barnes, P., Cox, S., Norris, R., et al. (2014). A model of active faulting in New Zealand. *New Zealand Journal of Geology and Geophysics*, *57*(1), 32–56. https://doi.org/10.1080/00288306.2013.854256

Little, T. A., & Roberts, A. P. (1997). Distribution and mechanism of neogene to present-day vertical axis rotations, Pacific-Australian plate boundary zone, South Island, New Zealand. *Journal of Geophysical Research*, *102*(B9), 20447–20468. https://doi.org/10.1029/97jb01279

Lomax, A., Virieux, J., Volant, P., & Berge-Thierry, C. (2000). Probabilistic earthquake location in 3D and layered models. In *Advances in seismic event location* (pp. 101–134). Springer. https://doi.org/10.1007/978-94-015-9536-0_5

Maggi, A., Tape, C., Chen, M., Chao, D., & Tromp, J. (2009). An automated time-window selection algorithm for seismic tomography. *Geophysical Journal International*, *178*(1), 257–281. https://doi.org/10.1111/j.1365-246x.2009.04099.x

Marquering, H., Dahlen, F., & Nolet, G. (1999). Three-dimensional sensitivity kernels for finite-frequency traveltimes: The banana-doughnut paradox. *Geophysical Journal International*, *137*(3), 805–815. https://doi.org/10.1046/j.1365-246x.1999.00837.x

Miyoshi, T., Obayashi, M., Peter, D., Tono, Y., & Tsuboi, S. (2017). Adjoint tomography of the crust and upper mantle structure beneath the Kanto region using broadband seismograms. *Progress in Earth and Planetary Science*, *4*(1), 1–20. https://doi.org/10.1186/s40645-017-0143-8

Mochizuki, K., Sutherland, R., Henrys, S., Bassett, D., Van Avendonk, H., Arai, R., et al. (2019). Recycling of depleted continental mantle by subduction and plumes at the Hikurangi Plateau large igneous province, Southwestern Pacific Ocean. *Geology*, *47*(8), 795–798. https://doi.org/10.1130/g46250.1

Modrak, R., Borisov, D., Lefebvre, M., & Tromp, J. (2018). SeisFlows — flexible waveform inversion software. *Computers & Geosciences*, *115*, 88–95. https://doi.org/10.1016/j.cageo.2018.02.004

Modrak, R., & Tromp, J. (2016). Seismic waveform inversion best practices: Regional, global and exploration test cases. *Geophysical Journal International*, *206*(3), 1864–1889. https://doi.org/10.1093/gji/ggw202

Montelli, R., Nolet, G., Dahlen, F., Masters, G., Engdahl, E. R., & Hung, S.-H. (2004). Finite-frequency tomography reveals a variety of plumes in the mantle. *Science*, *303*(5656), 338–343. https://doi.org/10.1126/science.1092485

Mortimer, N. (2004). New Zealand's geological foundations. *Gondwana Research*, *7*(1), 261–272. https://doi.org/10.1016/s1342-937x(05)70324-5

Mortimer, N., & Parkinson, D. (1996). Hikurangi Plateau: A cretaceous large igneous province in the Southwest Pacific Ocean. *Journal of Geophysical Research*, *101*(B1), 687–696. https://doi.org/10.1029/95jb03037

Nazarian, S., & Stokoe, K. H. (1984). Nondestructive testing of pavements using surface waves. *Transportation Research Record*, *993*, 67–79.

Nicol, A., & Beavan, J. (2003). Shortening of an overriding plate and its implications for slip on a subduction thrust, central Hikurangi Margin, New Zealand. *Tectonics*, *22*(6). https://doi.org/10.1029/2003tc001521

Nicol, A., Mazengarb, C., Chanier, F., Rait, G., Uruski, C., & Wallace, L. (2007). Tectonic evolution of the active Hikurangi subduction margin, New Zealand, since the Oligocene. *Tectonics*, *26*(4). https://doi.org/10.1029/2006tc002090

Nocedal, J., & Wright, S. (2006). *Numerical optimization*. Springer Science & Business Media.

Nolet, G. (2008). *A breviary of seismic tomography*. https://doi.org/10.1017/cbo9780511984709

Pondard, N., & Barnes, P. M. (2010). Structure and paleoearthquake records of active submarine faults, Cook Strait, New Zealand: Implications for fault interactions, stress loading, and seismic hazard. *Journal of Geophysical Research*, *115*(B12). https://doi.org/10.1029/2010jb007781

Reyners, M., Eberhart-Phillips, D., & Bannister, S. (2011). Tracking repeated subduction of the Hikurangi Plateau beneath New Zealand. *Earth and Planetary Science Letters*, *311*(1–2), 165–171. https://doi.org/10.1016/j.epsl.2011.09.011

Reyners, M., Eberhart-Phillips, D., & Bannister, S. (2017). Subducting an old subduction zone sideways provides insights into what controls plate coupling. *Earth and Planetary Science Letters*, *466*, 53–61. https://doi.org/10.1016/j.epsl.2017.03.004

Reyners, M., Eberhart-Phillips, D., Stuart, G., & Nishimura, Y. (2006). Imaging subduction from the trench to 300 km depth beneath the central North Island, New Zealand, with Vp and Vp/Vs. *Geophysical Journal International*, *165*(2), 565–583. https://doi.org/10.1111/j.1365-246x.2006.02897.x

Ristau, J. (2008). Implementation of routine regional moment tensor analysis in New Zealand. *Seismological Research Letters*, *79*(3), 400–415. https://doi.org/10.1785/gssrl.79.3.400

Ristau, J. (2013). Update of regional moment tensor analysis for earthquakes in New Zealand and adjacent offshore regions. *Bulletin of the Seismological Society of America*, *103*(4), 2520–2533. https://doi.org/10.1785/0120120339

Ruan, Y., Lei, W., Modrak, R., Örsvuran, R., Bozdağ, E., & Tromp, J. (2019). Balancing unevenly distributed data in seismic tomography: A global adjoint tomography example. *Geophysical Journal International*, *219*(2), 1225–1236. https://doi.org/10.1093/gji/ggz356

Sherburn, S., & White, R. S. (2006). Tectonics of the Taranaki region, New Zealand: Earthquake focal mechanisms and stress axes. *New Zealand Journal of Geology and Geophysics*, *49*(2), 269–279. https://doi.org/10.1080/00288306.2006.9515165

Sherburn, S., White, R. S., & Chadwick, M. (2006). Three-dimensional tomographic imaging of the Taranaki volcanoes, New Zealand. *Geophysical Journal International*, *166*(2), 957–969. https://doi.org/10.1111/j.1365-246x.2006.03040.x

Stagpoole, V., Miller, C., Caratori Tontini, F., Brakenrig, T., & Macdonald, N. (2020). A two million-year history of rifting and caldera volcanism imprinted in new gravity anomaly compilation of the Taupō Volcanic Zone, New Zealand. *New Zealand Journal of Geology and Geophysics*, 1–14. https://doi.org/10.1080/00288306.2020.1848882

Stern, T. (1985). A back-arc basin formed within continental lithosphere: The central volcanic region of New Zealand. *Tectonophysics*, *112*(1–4), 385–409. https://doi.org/10.1016/0040-1951(85)90187-8

Sutherland, R., Eberhart-Phillips, D., Harris, R., Stern, T., Beavan, J., Ellis, S., et al. (2007). Do great earthquakes occur on the Alpine Fault in central South Island, New Zealand? *Geophysical Monagraph - American Geophysical Union*, *175*, 237.

Tao, K., Grand, S. P., & Niu, F. (2018). Seismic structure of the upper mantle beneath Eastern Asia from full waveform seismic tomography. *Geochemistry, Geophysics, Geosystems*, *19*(8), 2732–2763. https://doi.org/10.1029/2018gc007460

Tape, C., Liu, Q., Maggi, A., & Tromp, J. (2010). Seismic tomography of the Southern California crust based on spectral-element and adjoint methods. *Geophysical Journal International*, *180*(1), 433–462. https://doi.org/10.1111/j.1365-246x.2009.04429.x

Tape, C., Liu, Q., & Tromp, J. (2007). Finite-frequency tomography using adjoint methods—methodology and examples using membrane surface waves. *Geophysical Journal International*, *168*(3), 1105–1129. https://doi.org/10.1111/j.1365-246x.2006.03191.x

Tarantola, A. (1984). Inversion of seismic reflection data in the acoustic approximation. *Geophysics*, *49*(8), 1259–1266. https://doi.org/10.1190/1.1441754

Tarantola, A. (2005). *Inverse problem theory and methods for model parameter estimation* (Vol. 89). Siam.

Taylor, B. (2006). The single largest oceanic plateau: Ontong Java–Manihiki–Hikurangi. *Earth and Planetary Science Letters*, *241*(3–4), 372–380. https://doi.org/10.1016/j.epsl.2005.11.049

Townend, J., Sherburn, S., Arnold, R., Boese, C., & Woods, L. (2012). Three-dimensional variations in present-day tectonic stress along the Australia–Pacific plate boundary in New Zealand. *Earth and Planetary Science Letters*, *353*, 47–59. https://doi.org/10.1016/j.epsl.2012.08.003

Tromp, J., Tape, C., & Liu, Q. (2005). Seismic tomography, adjoint methods, time reversal and banana-doughnut kernels. *Geophysical Journal International*, *160*(1), 195–216.

Ukawa, M., & Fukao, Y. (1981). Poisson's ratios of the upper and lower crust and the sub-Moho mantle beneath Central Honshu, Japan. *Tectonophysics*, *77*(3–4), 233–256. https://doi.org/10.1016/0040-1951(81)90265-1

Uruski, C. (1992). *Sedimentary basins and structure of Cook Strait. Report 92/03*. Institute of Geological and Nuclear Sciences Science.

Villamor, P., & Berryman, K. (2006). Evolution of the southern termination of the Taupō rift, New Zealand. *New Zealand Journal of Geology and Geophysics*, *49*(1), 23–37. https://doi.org/10.1080/00288306.2006.9515145

Villamor, P., Berryman, K., Ellis, S., Schreurs, G., Wallace, L., Leonard, G., et al. (2017). Rapid evolution of subduction-related continental intraarc rifts: The Taupo Rift, New Zealand. *Tectonics*, *36*(10), 2250–2272. https://doi.org/10.1002/2017tc004715

Wallace, L. (2020). Slow slip events in New Zealand. *Annual Review of Earth and Planetary Sciences*, *48*, 175–203. https://doi.org/10.1146/annurev-earth-071719-055104

Wallace, L., Barnes, P., Beavan, J., Van Dissen, R., Litchfield, N., Mountjoy, J., et al. (2012). The kinematics of a transition from subduction to strike-slip: An example from the central New Zealand plate boundary. *Journal of Geophysical Research*, *117*(B2). https://doi.org/10.1029/2011jb008640

Wallace, L., & Beavan, J. (2006). A large slow slip event on the central Hikurangi subduction interface beneath the Manawatu region, North Island, New Zealand. *Geophysical Research Letters*, *33*(11). https://doi.org/10.1029/2006gl026009

Wallace, L., Beavan, J., Bannister, S., & Williams, C. (2012). Simultaneous long-term and short-term slow slip events at the Hikurangi subduction margin, New Zealand: Implications for processes that control slow slip event occurrence, duration, and migration. *Journal of Geophysical Research*, *117*(B11). https://doi.org/10.1029/2012jb009489

Wallace, L., Beavan, J., McCaffrey, R., Berryman, K., & Denys, P. (2007). Balancing the plate motion budget in the South Island, New Zealand using GPS, geological and seismological data. *Geophysical Journal International*, *168*(1), 332–352. https://doi.org/10.1111/j.1365-246x.2006.03183.x

Wallace, L., Beavan, J., McCaffrey, R., & Darby, D. (2004). Subduction zone coupling and tectonic block rotations in the North Island, New Zealand. *Journal of Geophysical Research*, *109*(B12). https://doi.org/10.1029/2004jb003241

Wallace, L., Cochran, U. A., Power, W. L., & Clark, K. J. (2014). Earthquake and tsunami potential of the Hikurangi subduction thrust, New Zealand: Insights from paleoseismology, GPS, and tsunami modeling. *Oceanography*, *27*(2), 104–117. https://doi.org/10.5670/oceanog.2014.46

Wallace, L., Reyners, M., Cochran, U., Bannister, S., Barnes, P., Berryman, K., et al. (2009). Characterizing the seismogenic zone of a major plate boundary subduction thrust: Hikurangi Margin, New Zealand. *Geochemistry, Geophysics, Geosystems*, *10*(10). https://doi.org/10.1029/2009GC002610

Webb, S. C. (1998). Broadband seismology and noise under the ocean. *Reviews of Geophysics*, *36*(1), 105–142. https://doi.org/10.1029/97rg02287

Williams, C., Eberhart-Phillips, D., Bannister, S., Barker, D., Henrys, S., Reyners, M., et al (2013). Revised interface geometry for the Hikurangi subduction zone, New Zealand. *Seismological Research Letters*, *84*(6), 1066–1073. https://doi.org/10.1785/0220130035

Williams, C., & Wallace, L. (2018). The impact of realistic elastic properties on inversions of shallow subduction interface slow slip events using seafloor geodetic data. *Geophysical Research Letters*, *45*(15), 7462–7470. https://doi.org/10.1029/2018gl078042

Wilson, C., Gravley, D., Leonard, G., & Rowland, J. (2009). Volcanism in the central Taupō volcanic zone, New Zealand: Tempo, styles and controls. In *Studies in volcanology: the Legacy of George Walker* (Vol. 2, pp. 225–247). Special Publications of IAVCEI.

Wilson, C., Houghton, B., McWilliams, M., Lanphere, M., Weaver, S., & Briggs, R. (1995). Volcanic and structural evolution of Taupo Volcanic Zone, New Zealand: A review. *Journal of Volcanology and Geothermal Research*, *68*(1–3), 1–28. https://doi.org/10.1016/0377-0273(95)00006-g

Yuan, Y. O., Bozdağ, E., Ciardelli, C., Gao, F., & Simons, F. J. (2020). The exponentiated phase measurement, and objective-function hybridization for adjoint waveform tomography. *Geophysical Journal International*, *221*(2), 1145–1164. https://doi.org/10.1093/gji/ggaa063

Zhao, L., Jordan, T. H., & Chapman, C. H. (2000). Three-dimensional Fréchet differential kernels for seismicdelay times. *Geophysical Journal International*, *141*(3), 558–576. https://doi.org/10.1046/j.1365-246x.2000.00085.x

Zhu, H., Bozdağ, E., & Tromp, J. (2015). Seismic structure of the European upper mantle based on adjoint tomography. *Geophysical Journal International*, *201*(1), 18–52. https://doi.org/10.1093/gji/ggu492